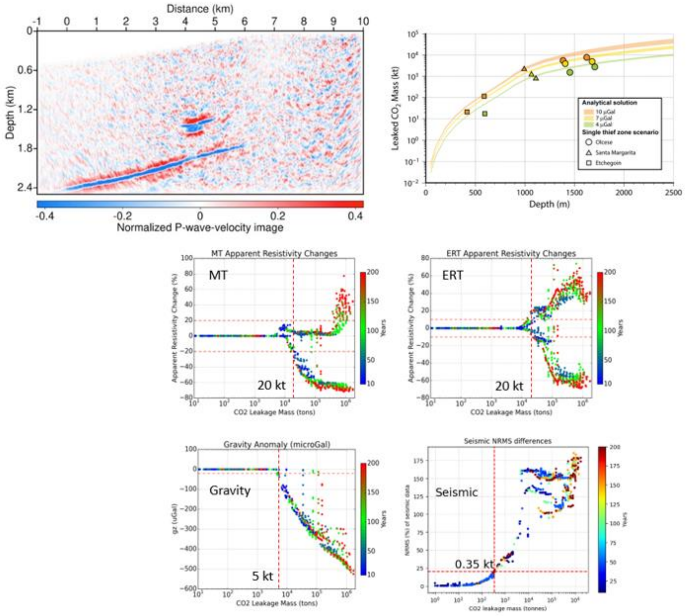

Detection Thresholds and Sensitivities of Geophysical Techniques for CO_2 Plume Monitoring

11 December 2020

Office of Fossil Energy

NRAP-TRS-I-001-2020

DOE/NETL-2021/2638

Disclaimer

Cover Illustration: Evaluation of detection thresholds of multiple techniques on various scales.

Suggested Citation: Gasperikova, E.; Daley, T.; Appriou, D.; Bonneville, A.; Feng, Z.; Huang, L.; Yang, X.; Wang, Z.; Dilmore, R.; Gao, K. *Detection Thresholds and Sensitivities of Geophysical Techniques for CO_2 Plume Monitoring*; NRAP-TRS-I-001-2020; DOE.NETL-2021.2638; NRAP Technical Report Series; U.S. Department of Energy, National Energy Technology Laboratory: Pittsburgh, PA, 2020; p 64. DOI: 10.2172/1735331.

An electronic version of this report can be found at:

https://edx.netl.doe.gov/nrap

Detection Thresholds and Sensitivities of Geophysical Techniques for CO_2 Plume Monitoring

Erika Gasperikova[1], Thomas Daley[1], Delphine Appriou[2], Alain Bonneville[2], Zongcai Feng[3], Lianjie Huang[3], Xianjin Yang[4], Zan Wang[5], Robert Dilmore[5], Kai Gao[3]

[1] **Lawrence Berkeley National Laboratory, 1 Cyclotron Road, Berkeley, CA 94720**

[2] **Pacific Northwest National Laboratory902 Battelle Boulevard, Richland, WA 99354**

[3] **Los Alamos National Laboratory, Bikini Atoll Road, SM 30, Los Alamos, NM 87545**

[4] **Lawrence Livermore National Laboratory, 7000 East Avenue, Livermore, CA 94551**

[5] **National Energy Technology Laboratory, 626 Cochrans Mill Road, Pittsburgh, PA 15236**

NRAP-TRS-I-001-2020

DOE/NETL-2021/2638

Level I Technical Report Series

11 December 2020

This page intentionally left blank.

Table of Contents

EXECUTIVE SUMMARY 1

1. INTRODUCTION..3

2. SURFACE SEISMIC MONITORING 4
  2.1 SURFACE SEISMIC MONITORING..4
  2.2 SURFACE SEISMIC DETECTION CAPABILITIES 5

3. MONITORING USING VERTICAL SEISMIC PROFILING..18
  3.1 BACKGROUND 18
  3.2 CO_2 MONITORING APPLICATIONS 19
  3.3 DETECTION AND QUANTIFICATION OF CO_2 FROM VSP SURVEYS 19
  3.4 LIMITATIONS ON QUANTITATIVE INTERPRETATION 22

4. GRAVITY MONITORING 27
  4.1 BACKGROUND 27
  4.2 SURFACE GRAVITY..28
  4.3 BOREHOLE GRAVITY 32

5. ELECTRICAL AND ELECTROMAGNETIC MONITORING..40
  5.1 BACKGROUND 40
  5.2 EM MONITORING FOR RESISTIVE TARGETS..42
  5.3 EM MONITORING FOR CONDUCTIVE TARGETS..46

6. SUMMARY 49

7. REFERENCES..51

List of Figures

Figure 1: 4D seismic monitoring for the Sleipner storage project. Upper left shows a schematic of the injection into the Utsira formation with the rising buoyant CO_2 plume....4

Figure 2: Size of 1,000 tonne accumulations as a function of depth below the surface for CO_2 saturation of (a) 5%, (b) 10%, and (c) 20%. 6

Figure 3: Differences between migrated sections for the initial conditions and 1,000 tonne CO_2 accumulations at depths of (a) 500 m, (b) 800 m, (c) 1,000 m, and (d) 1,300 m....7

Figure 4: Change in (a) CO_2 saturation, (b) P-wave, (c) S-wave velocities, and (d) signal amplitude due to the CO_2 plume at the depth of 1,000 m.. 9

Figure 5: Amplitude difference in migrated depth sections using (a) 25 m and (b) 10 m shot intervals. 10

Figure 6: Maximum NRMS (in %) as a function of time and various survey parameters. 10

Figure 7: Detection threshold as a function of signal-to-noise ratio. 11

Figure 8: NRMS difference of seismic data as a function of CO_2 leakage mass. Colors represent time steps. 12

Figure 9: NRMS difference in seismic data as a function of cumulative CO_2 leakage mass. Colors represent different depth intervals. 12

Figure 10: Amplitude change plotted as a function of CO_2 saturation. Colors and symbols illustrate the relationship with the depth and size of the plume. 13

Figure 11: (a) Normalized P-wave velocity image difference and (b) true model difference for a small CO_2 plume at 1,500 m depth demonstrate a great agreement and powerful tool for CO_2 plume detection. 14

Figure 12: True and normalized inverted (bottom left) P-wave velocity image difference, true and normalized inverted density image difference, obtained using explosive sources for a 2D slice of the Kimberlina 2 model. 15

Figure 13: Examples of inverted P-wave impedance, S-wave impedance, and density from a 9-component 3D dataset in northern Montana. 16

Figure 14: Normalized inverted P-wave velocity image difference and density image difference obtained using multi-component data and vertical sources for a 2D slice of the Kimberlina 2 model. 17

Figure 15: Examples of VSP acquisition geometries. 18

Figure 16: Time-lapse change in observed seismic reflection amplitude from the Frio project. 20

Figure 17: Horizontal slice of VSP reflection change (nRMS) within the Deadwood reservoir level (Aquistore) for 3D-VSP at CO_2 injection amounts of (a) 36,000 and (b) 102,000 tonnes, respectively. 21

List of Figures (cont.)

Figure 18: (a) Interpretation of OVSP data from Cranfield showing NRMS values, and change in reflection amplitude for top and base of reservoir; (b) the predicted change in reflection amplitude (both numerical and analytic) for top and base of reservoir. 21

Figure 19: CO_2 saturation values from the Weyburn 3D VSP analysis for a horizontal cross section in the reservoir zone 22

Figure 20: Maps of RMS amplitudes of the time-lapse signal obtained for monitoring surveys M1–M5 in 24 ms time window centered at 1,210 ms (corresponding to the injection interval). 23

Figure 21: Effective plume diameter detectable for different signal quality cut-offs (as a function of the threshold N) for 30,0000 tonnes of CO_2/CH_4 at Otway Stage 2. 24

Figure 22: Effective diameter of detectability for injection volumes of 10, 15, and 30 kt as a function of the threshold N (a measure of SNR and detectability). 24

Figure 23: Total plume mass, either falsely detected or not detected, vs. seismic response (change in acoustic impedance) shown as a bar graph, along with plume area missed (not detected) vs. acoustic impedance change. 26

Figure 24: Change in density as a function of depth. 27

Figure 25: CO_2 saturation (a, c, e), and CO_2 mass (b, d, f) as functions of depth for a variable cylinder radius. The detection threshold is 4 μGal in (a) and (b), 7 μGal in (c) and (d), and 10 μGal in (e) and (f). 29

Figure 26: CO_2 plume radius (a, c, e), and CO_2 mass (b, d, f) as functions of depth for a variable CO_2 saturation. The detection threshold is 4 μGal in (a) and (b), 7 μGal in (c) and (d), and 10 μGal in (e) and (f). 31

Figure 27: CO_2 wedge model. 32

Figure 28: Borehole gravity response of the model in Figure 27a as a function of distance from the wedge edge. 33

Figure 29: Conceptual model for borehole gravity measurements calculations. 33

Figure 30: 3D gravity change of the horizontal component g_x induced by 10 kt of CO_2 plume represented by a horizontal prism located in x=0, y=0 and z=410 m and 50% CO_2 saturation. 34

Figure 31: Maximum distance of detection vs. depth of a 5-μGal change in the vertical gravity component g_z for (a) 10 kt, (b) 20 kt, (c) 30 kt, (d) 40 kt, (e) 50 kt, and (f) 100 kt CO_2 mass and CO_2 saturations varying from 0.05 to 0.5 (5–50%) 36

Figure 32: Maximum distance of detection vs. depth of a 5-μGal change in the horizontal gravity component g_x for (a) 10 kt, (b) 20 kt, (c) 30 kt, (d) 40 kt, (e) 50 kt, and (f) 100 kt CO_2 mass and CO_2 saturations varying from 0.05 to 0.5 (5–50%). 37

List of Figures (cont.)

Figure 33: Maximum distance of detection vs. depth of a 10-μGal change in the vertical gravity component g_z for (a) 10 kt, (b) 20 kt, (c) 30 kt, (d) 40 kt, (e) 50 kt, and (f) 100 kt CO_2 mass and CO_2 saturations varying from 0.05 to 0.5 (5–50%) 38

Figure 34: Maximum distance of detection vs. depth of a 10-μGal change in the horizontal gravity component g_x for (a) 10 kt, (b) 20 kt, (c) 30 kt, (d) 40 kt, (e) 50 kt, and (f) 100 kt CO_2 mass and CO_2 saturations varying from 0.05 to 0.5 (5–50%).................39

Figure 35: Fluid resistivity as a function of NaCl concentration and temperature.......................41

Figure 36: Rock bulk resistivity (ρ_b) as a function of CO_2 saturation (S_{CO2}). Pore fluid resistivity is 0.3 Ohm-m, porosity is 35%, a =1, m = 2, and n=2. 41

Figure 37: Apparent resistivity response of 1,000 Ohm-m and 50-m thick layer in a 100 Ohm-m half-space as a function of layer depth. 42

Figure 38: (a) Model with CO_2 plumes at different depths, (b) surface responses, and (c) borehole-to-surface responses due to CO_2 plumes in (a). 43

Figure 39: (a) Deep CO_2 plume model, (b) changes in subsurface resistivity due to CO_2 presence at time-3, (c) changes in measured responses at three different times using borehole-to-surface configuration. 44

Figure 40: 2D EM inversion of synthetic data. 45

Figure 41: Contour plots of TDS increase above background (top) and CO_2 saturation (bottom) are shown at 50 years for a leaking well 1 km from the CO_2 injector, a high groundwater gradient, high wellbore permeability, and two leaky aquifers..........................46

Figure 42: Apparent resistivity change as a function of CO_2 leakage mass for (a) ERT and (b) MT. 47

Figure 43: Change is resistivity as a function of CO_2 saturation for (a) ERT and (b) MT. 48

List of Tables

Table 1: Depths, temperatures, pressure, and CO_2 density used in the calculations 5

Acronyms, Abbreviations, and Symbols

Term	Description
2D	Two-dimensional
3D	Three-dimensional
4D	Four-dimensional, time being the fourth dimension
B, H	Magnetic field
CCS	Carbon capture and sequestration
CSEM	Controlled source electromagnetics
CO_2	Carbon dioxide
DAS	Distributed acoustic sensing
E	Electric field
EM	Electromagnetic
EOR	Enhanced oil recovery
ERT	Electrical resistance tomography
GCS	Geologic carbon storage
LSRTM	Least-squares reverse-time migration
MT	Magnetotellurics
NRMS	Normalized root mean square
OVSP	Offset vertical seismic profiling
PP	P-wave to P-wave reflections
PS	Converted P-wave to S-wave
SNR	Signal-to-noise ratio
SS	Converted S-wave to S-wave
TDS	Total dissolved solids
VSP	Vertical seismic profile

Acknowledgments

This work was completed as part of National Risk Assessment Partnership (NRAP) project. Support for this project comes from the U.S. Department of Energy (DOE) Office of Fossil Energy's Crosscutting Research Program. Work at Lawrence Berkeley National Laboratory was completed under the U.S. DOE Contract No. DE-AC02-05CH1123. Work at National Energy Technology Laboratory was performed under Field Work Proposal No. 1022407. Work at Los Alamos National Laboratory was supported under the U.S. DOE Contract No. DE-AC52-06NA25396. Work at Pacific Northwest National Laboratory was supported under the U.S. DOE Contract No. DE-AC05-76RL01830. Work at Lawrence Livermore National Laboratory was performed under the U.S. DOE Contract No. DE-AC52-07NA27344.

EXECUTIVE SUMMARY

This report assesses capabilities and limitations of different geophysical techniques for monitoring geologic sequestration of CO_2. Seismic, gravity, electrical, and electromagnetic (EM) techniques are considered. Monitoring approaches for site characterization prior to CO_2 injection are different from those used while injecting CO_2, or those suitable for post-injection monitoring. The focus of this study is on the aspects relevant to long-term monitoring of large areas in the post-injection phase, and specifically on early detection of secondary CO_2 plumes.

Each of the techniques is sensitive to a different subsurface property. Seismic velocity depends on the bulk and shear modulus and density, whereas the gravity response depends on density, and the electrical response depends on resistivity. Each of these geophysical properties are in and of themselves sensitive to changes in formation properties such as porosity, pore fluid, and fluid saturation. For this reason, these techniques are complementary to each other, and when used together could provide improved characterization of the subsurface. This assessment is based on several model scenarios. Some examples are given for monitoring during injection, as those are the only examples with demonstrated performance in field conditions.

Surface seismic monitoring is generally the key monitoring tool for CO_2 storage projects. The use of time-lapse seismic to monitor a CO_2 plume has been best demonstrated by the Sleipner project, which has been conducting three-dimensional (3D) seismic surveys since the mid-1990s. This current study focuses on early detection of secondary CO_2 plumes, which means imaging much smaller volumes of CO_2 than in the case of Sleipner. Sensitivity studies have been conducted to assess the influence of accumulation thickness, saturation, and the presence of accumulations at multiple depths. Models also included the change from supercritical to gas phase when CO_2 moves to shallower than 800-m depth, when the density decreases and the compressibility increases, which significantly improves seismic detection limits. Numerical models were used to assess the importance of survey geometry, source characteristic, receiver types, and an influence of noise present in the data when establishing detection limits. The size of the secondary CO_2 plume that is detectable strongly depends on the survey geometry, field conditions, rock properties, and data processing or imaging.

Vertical seismic profiling (VSP) is an established tool for imaging and monitoring in the vicinity of accessible boreholes (those which can be entered for sensor deployment). Typically, VSP offers improved spatial resolution and lower cost, as compared to surface seismic. The applicability of VSP to CO_2 storage monitoring has been well established by many projects. The use of permanent fiber deployment in a well offers very low-cost, highly repeatable VSPs using distributed acoustic sensing (DAS). For long-term monitoring, the advantages of permanent DAS are considerable. The signal-to-noise ratio gap between convectional sensors and DAS technology is closing rapidly. It is also likely that large scale projects would use multiple wells, in contrast to small-scale CO_2 projects that used a single monitoring well, near the injection well, for VSP. In this way, VSP can provide a method of monitoring CO_2 plumes as they grow or migrate.

Earlier numerical studies demonstrated that time-lapse gravity could be successfully used as a monitoring tool for a geologic carbon storage (GCS) site. The first deployment of this kind at the Sleipner site allowed gravity anomalies larger than 10 μGal to be detected, and constrained the density of the injected CO_2 and the rate of dissolution. For deep CO_2 storage projects, the error associated with gravity surveys (typically 5 μGal) limits the performance of surface

measurements. To overcome this challenge and obtain stronger gravity responses, borehole gravity surveys have been suggested. While these were assessed numerically, only a limited number of field tests have been undertaken, e.g., at the Cranfield site, Mississippi.

With recent engineering advances in gravimeter technology, both for surface and borehole deployments, the landscape regarding the use of time-lapse gravity measurements as an efficient and cost-effective method for monitoring subsurface processes may change. Detection of gravity variations accompanying mass redistributions in the subsurface caused by fluid movements provides a unique means for monitoring the GCS site dynamics. The gravity method is the only geophysical method that can provide a direct estimate of CO_2 mass distribution at depth.

A decision whether gravity would be included in a monitoring portfolio will be site specific, and depend on an expected size and depth of the CO_2 plume of interest. The gravity response is inversely proportional to the squared distance, hence the closer the sensors are to the CO_2 plume, the smaller the plume size that can be detected.

Electrical and EM techniques infer the distribution of electrical resistivity in the subsurface from measured electric and magnetic fields. The electrical resistivity of the subsurface is highly sensitive to changes in formation properties such as porosity, pore fluid resistivity, and fluid saturation. These techniques are much more sensitive to low resistivities (conductive targets), with the response to a shallow conductive target being an order of magnitude larger than the one to the deep resistive target. Hence, deep CO_2 plumes (resistive targets) are much more difficult to detect. There are many possible configurations of sources (transmitters) and receivers (sensors) that would provide required sensitivity for these targets. Depth and size of the secondary CO_2 plume will again play an important role in the site specific, fit-for-purpose, monitoring array design.

The aim of this study is to provide a framework of up-to-date information which can be utilized to start the process of designing an optimal monitoring network. The size of the secondary CO_2 plume that is detectable strongly depends on the survey geometry, field conditions, rock properties, and data processing. The cost is also dependent on survey geometry, field conditions and processing needed. The trade-off between sensitivity to an expected plume size and cost is expected to play an important role in designing monitoring arrays at GCS sites.

1. INTRODUCTION

The purpose of this study is to assess sensitivities and detection thresholds of geophysical techniques when used to monitor CO_2 plume movements. Seismic, gravity, electrical, and electromagnetic (EM) techniques are considered. Different monitoring approaches are suitable for a site characterization prior to CO_2 injection, for monitoring while injecting CO_2, or for a post-injection stage. Each of the techniques is sensitive to a different subsurface property. Seismic velocity depends on the bulk and shear modulus and density, whereas gravity response depends on density, and electrical resistivity is sensitive to changes in fluid properties. Each of these geophysical properties are in and of themselves sensitive to changes in formation properties such as porosity, pore fluid, and fluid saturation. For this reason, these techniques are complementary to each other, and when used together could provide improved characterization of the subsurface. Separate publications have been written about each of these techniques. The focus of this study is on the aspects relevant to long-term monitoring of large areas that would be suitable for the post-injection phase. This assessment is based on several model scenarios. Some examples are given for monitoring during the injection, as those are the only examples with demonstrated performance in field conditions. The aim of this study is to provide a framework of up-to-date information which can be utilized to start the process of designing an optimal monitoring network.

2. SURFACE SEISMIC MONITORING

Surface seismic monitoring is generally the key monitoring tool for CO_2 storage projects. This technique utilizes elastic wave propagation in the subsurface to determine changes in its physical properties. Seismic surveys are done either along profiles (two-dimensional, 2D) or over an area (three-dimensional, 3D). The data are processed to generate images of reflecting interfaces or horizons, and then analyzed for the properties of those horizons that can be related to rock properties using theoretical or empirical relationships. When 3D seismic surveys are used for repeated (time-lapse) monitoring of the same site, it is called four-dimensional (4D) seismic (time being the fourth dimension).

2.1 SURFACE SEISMIC MONITORING

The use of 4D seismic to monitor injected CO_2 is best demonstrated by the Sleipner project, which has been conducting 3D seismic surveys over an increasing volume of injected CO_2 since the mid-1990s (e.g., Chadwick et al., 2010; Chadwick and Noy, 2015; Furre et al., 2017). An example of the Sleipner results is shown in Figure 1 with 2D vertical slices of the 3D data shown on the right, and horizon slices through the upper-most layer containing CO_2 shown at lower left. Figure 1 shows results from seven surveys over 14 years (through 2008). Monitoring at the site continues to the present (Furre et al., 2017) with ten 3D seismic surveys and four gravity surveys acquired to date.

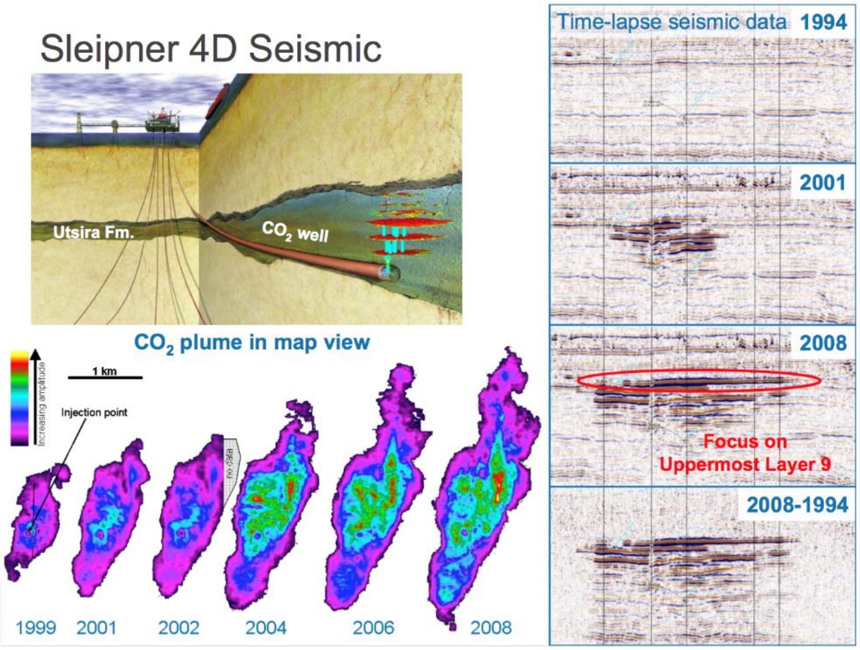

Figure 1: 4D seismic monitoring for the Sleipner storage project. Upper left shows a schematic of the injection into the Utsira formation with the rising buoyant CO_2 plume (blue and red). Right side figure shows a series of 2D vertical slices through the 3D data volume and through the injected CO_2 plume with the changing reflection amplitude clearly visible. The lower left is a series of horizon slices through the top layer containing CO_2 (layer 9 as indicated on the 2008 vertical slice) and plotted to show the interpreted extent of the amplitude change caused by CO_2 (purple, blue, green, and red indicate different reflection amplitude changes). Figure courtesy of P. Ringrose. See also Chadwick et al. (2010) and Furre et al. (2017).

The time-lapse seismic monitoring surveys from 1999 and 2001 immediately revealed the nature of the CO_2 plume in the reservoir. A number of separate reflective horizons were interpreted as thin layers of CO_2 trapped beneath the intra-reservoir mudstones, which were confirmed by a consecutive survey. This supported the hypothesis of a stable plume structure with discrete spreading layers, which were possible to map. Time-lapse seismic data contributed to improved understanding of plume evolution. Chadwick and Noy (2015) show that as more monitoring data were acquired through time, uncertainties about plume development were progressively reduced and predictive capabilities improved. Furre et al. (2017) demonstrated that combined interpretation of seismic and gravity monitoring surveys allowed for better quantification of the CO_2 mass changes and plume geometry.

2.2 SURFACE SEISMIC DETECTION CAPABILITIES

Several synthetic model scenarios were considered in investigating sensitivities or detection capabilities of surface seismic to detect CO_2 plume of variable size at different depths. This systematic study is an important step towards developing approaches for detecting leakage from the storage formation long before it could reach the groundwater formations or ground surface.

Scenario 1

A conceptual model used for this study assumes that CO_2 moves out from the storage reservoir, accumulates in a secondary trap above the storage horizon, and forms a cone-shaped plume. This is a reasonable assumption since as CO_2 migrates upward it is subject to buoyancy forces and capillary trapping. The size of the region containing CO_2 must be sufficient to generate an interpretable signal at the surface. Using a realistic geological model of the subsurface, calculations were made to assess the seismic response of accumulations of 1,000 tonnes of CO_2 at depths 500–2,000 m below the surface. A hydrostatic pore pressure gradient and lithostatic pressure increasing with a gradient of 22.6 kPa/m were assumed. The geothermal temperature gradient of 30°C/km was used. The density of the CO_2 was obtained using the NIST Mixture Property Database (1992). Calculated properties for selected depths are listed in Table 1.

Table 1: Depths, temperatures, pressure, and CO_2 density used in the calculations

Depth (m)	T (°C)	P (MPa)	CO_2 density (kg/m^3)	Phase
500	30	4.9	120.24	Gas
800	39	7.8	270.35	Supercritical
1,000	45	9.8	466.76	Supercritical
1,300	54	12.7	570.34	Supercritical
2,000	75	19.6	617.11	Supercritical

The secondary trap was a brine saturated unconsolidated sand layer with a thickness from 5 m to 100 m. The width of the plume was based on the size of the first Fresnel zone. The P-wave velocity of the shale was 2,700 m/s and its density 2,160 kg/m^3, while the sand P-wave velocity was 3,050 m/s and density 2,285 kg/m^3. The P-velocity of CO_2 plume was 2,530 m/s and its density 2,260 kg/m^3. The seismic wave center frequency was 30 Hz. For these conditions, the first Fresnel zone diameter is approximately 320 m. Calculations were carried out for plume widths of 0.5–2.0 Fresnel zones. Full 2D elastic seismic simulations were carried out with and without noise, followed by producing zero-offset stacked sections and Kirchhoff time migration.

Based on the densities, saturation, and thickness of the CO_2 accumulation, it is possible to calculate the radius of the cone-shaped accumulation. Plots of radius as a function of depth for a 1,000 tonne accumulation with a range of thicknesses and saturations are shown in Figure 2. As expected, as the accumulation moves towards the surface, it becomes significantly larger due to the associated decrease in density.

Sensitivity studies have been conducted to assess the influence of accumulation thickness, saturation, and the presence of accumulations at multiple depths. This model also includes the change from supercritical to gas phase when CO_2 moves to shallower than 800-m depth, when the density decreases and the compressibility increases, which significantly improves seismic detection limits.

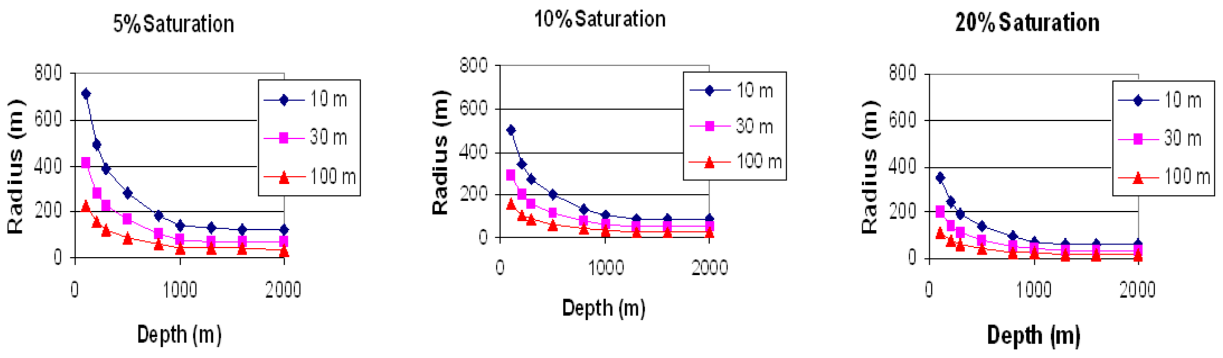

(a) (b) (c)

Figure 2: Size of 1,000 tonne accumulations as a function of depth below the surface for CO_2 saturation of (a) 5%, (b) 10%, and (c) 20%. Radius of CO_2 plume in 10, 30, and 100-m thick layers are shown in blue, magenta, and red, respectively.

At 2,000-m depth, the 5-m thick sand layer model produced no discernable reflection since the layer thickness was on the order of 5% of the seismic wavelength. The 10-m thick sand layer model generated a reflection, but none was observed at the location of the CO_2 plume. For the conditions assumed in this model, the impedance difference between the shale and the sand containing CO_2 was almost zero. The CO_2 plume in 30-m thick layer was imaged, where the reflections were generated at the interface between the brine and CO_2 saturated sand. There was a sufficient thickness of brine-saturated sand beneath the CO_2 wedge to generate a reflection. For these models the width of the plume was less than a Fresnel zone and the layer thickness was similar to or less than the layer tuning thickness. Even though the CO_2 plume was detected, interpretation of the reflection for fluid properties would be difficult because of geometric effects. A plume large enough to prevent contamination of reflections by geometrical effects had a width of about 480 m in a 100-m thick sand.

A key consideration in any study of what can be isolated from a background signal using numerical data is the assessment of the type and magnitude of noise present in the data. For the time-lapse monitoring approach considered, both static and dynamic noise was added to the data. The synthetic shot gathers with both the static and dynamic noise added were run through standard velocity analysis to determine interval velocities for normal move-out (NMO) corrections and Kirchhoff time migration. Figures 3a–d show the time-lapse differences between the response when the CO_2 plume was present and the initial conditions for 30-m thick plumes of CO_2 with a 20% saturation at depths of 500, 800, 1,000, and 1,300 m. While the accumulations at 500 m and 800 m are clearly detectable, at 1,000 m and 1,300 m, the response is of the same order as the noise and may be difficult to ascribe as a meaningful change in the section unless the signal-to-noise is reduced.

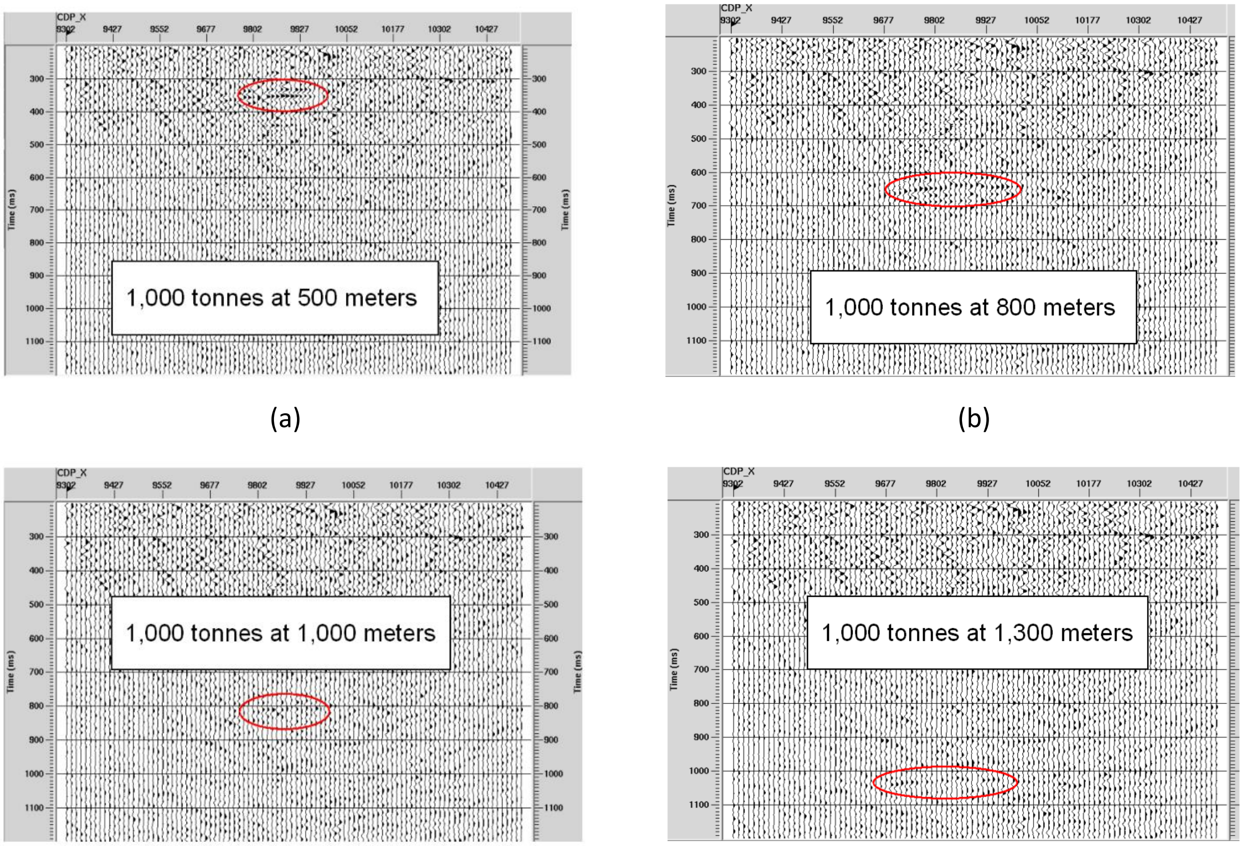

(a) (b)

(c) (d)

Figure 3: Differences between migrated sections for the initial conditions and 1,000 tonne CO_2 accumulations at depths of (a) 500 m, (b) 800 m, (c) 1,000 m, and (d) 1,300 m. A saturation of 20% is used for these calculations and the thickness of the cone-shaped accumulation is 30 m. The seismic response for the accumulation at depths of 500 m and 800 m is detectable; however, the response of the accumulation at depths of 1,000 m and 1,300 m are in the noise level of the survey.

Under favorable geological conditions, seismic methods are effective for detecting small accumulations of CO_2, particularly as the CO_2 moves closer to the ground surface. Once shallower than 800 m, the density decreases markedly and compressibility increases as CO_2 transitions from the supercritical phase to the gas phase. Both of these factors significantly improve the seismic detection limits for shallower accumulations. While these conclusions are dependent on the type and magnitude of the noise assumed, the noise levels used in this study are realistic or close to those that would be encountered on average for land acquisition. Because any assessment of the amounts of CO_2 that is detectable or any quantitative estimates of the quantity present is so dependent on the assumed noise levels, these assessments must be done on a site-specific basis. The design of seismic surveys for secondary CO_2 plume monitoring will be similar, but not necessarily the same as the design of surveys for time-lapse monitoring of oil and gas reservoirs. The latter case is concerned with mapping the changes within a reservoir at a known constant depth, while CO_2 plume monitoring must try to monitor the entire depth section. This will necessitate design of a wider aperture array for acquisition so that shallow portions of the section can be imaged as well as deeper portions.

Scenario 2

The second scenario was based on a synthetic FutueGen2 model. The CO_2 plume was at the depth of 1,000 m. Data were simulated using 2D survey line with shots every 25 m and receivers every 5 m, and 30 Hz Ricker source wavelet (Wang et al., 2018). Synthetic shot gathers were generated using the 2D acoustic finite-difference code. Figure 4 shows changes in CO_2 saturation, P-wave, and S-wave velocities, and the corresponding amplitude changes in the migrated depth section due to the CO_2 presence. These results suggest that this plume would not be detectable in the field.

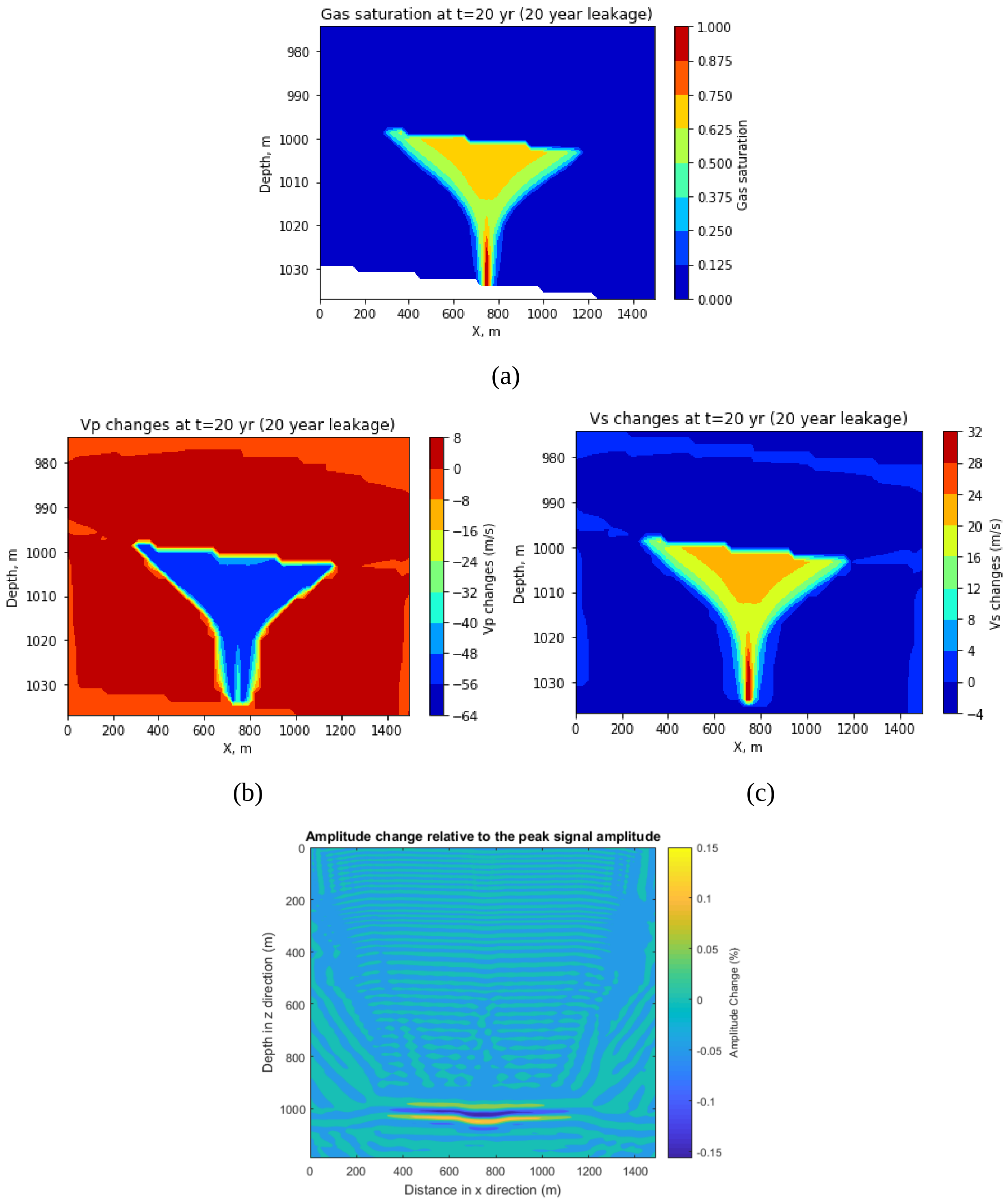

(a)

(b)

(c)

(d)

Figure 4: Change in (a) CO_2 saturation, (b) P-wave, (c) S-wave velocities, and (d) signal amplitude due to the CO_2 plume at the depth of 1,000 m. Figure from Wang et al. (2018).

The importance of survey geometry is illustrated in Figure 5. Again, using depth migrated sections, the amplitude difference with shot interval of 25 m is shown in Figure 5a, while the difference using 10-m shot intervals is shown in Figure 5b. Figure 6 illustrates that the shot spacing is decreased by 60%, a 30% increase occurs in the maximum of the normalized root-mean-square (NRMS) difference (Kragh and Christie, 2002). An additional parameter that may increase the NRMS amplitude is a source characteristic; the NRMS amplitude increases with a higher source center frequency.

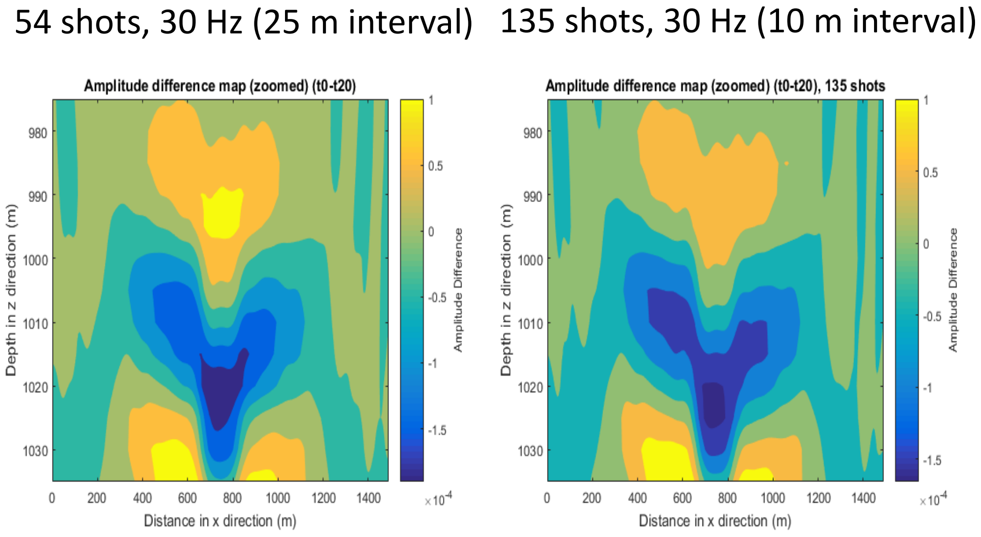

(a) (b)

Figure 5: Amplitude difference in migrated depth sections using (a) 25-m and (b) 10 m-shot intervals.

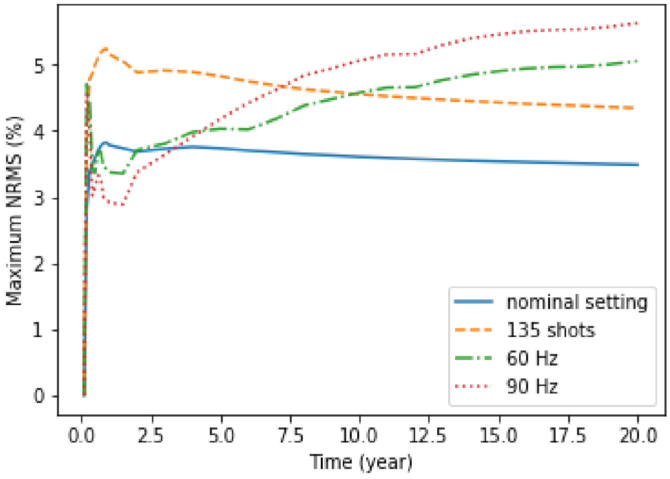

Figure 6: Maximum NRMS (in %) as a function of time and various survey parameters.

Figure 7 shows the relationship between the detection threshold and signal-to-noise ratio (SNR). The higher the SNR, the lower the detection threshold.

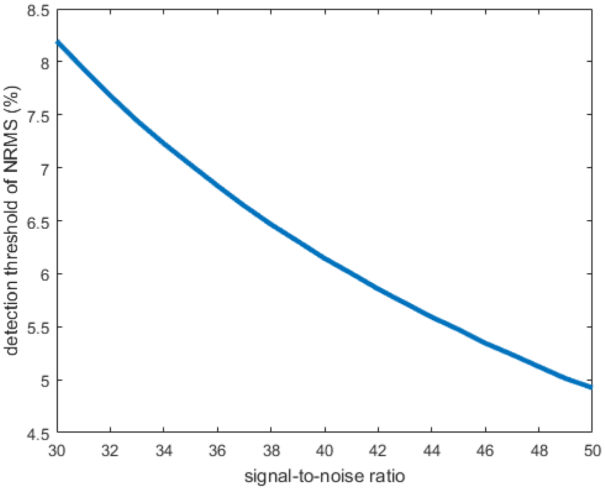

Figure 7: Detection threshold as a function of signal-to-noise ratio.

Scenario 3

The third synthetic model scenario was based on a hypothetical, commercial-scale geologic carbon storage (GCS) reservoir at the Kimberlina site in the southern San Joaquin Basin, 30 km northwest of Bakersfield, California, where CO_2 and brine leak through legacy wells into shallow aquifers. Over 900 aquifer impact datasets were used to capture uncertainty in the subsurface geology and leakage scenarios. Data were simulated along a 2D survey line with a shot spacing of 40 m and a receiver spacing of 5 m. Synthetic shot gathers were generated using a 2D acoustic-wave propagation code with a 30 Hz Ricker source wavelet. A sequence of seismic processing steps, including sorting to common-midpoint gathers, stacking, and post-stack migration, were applied to the data. The detectability of each simulated leakage scenario was evaluated by calculating the NRMS difference between the post-stack migrated images at different leakage stages and the baseline stage (i.e., without CO_2 leakage). The results are shown in Figure 8. A detection threshold of 20% NRMS difference was used in this study. The smallest detectable mass is indicated by the vertical dotted red line in Figure 8, indicating that the seismic method can detect a CO_2 leakage as small as 350 tons.

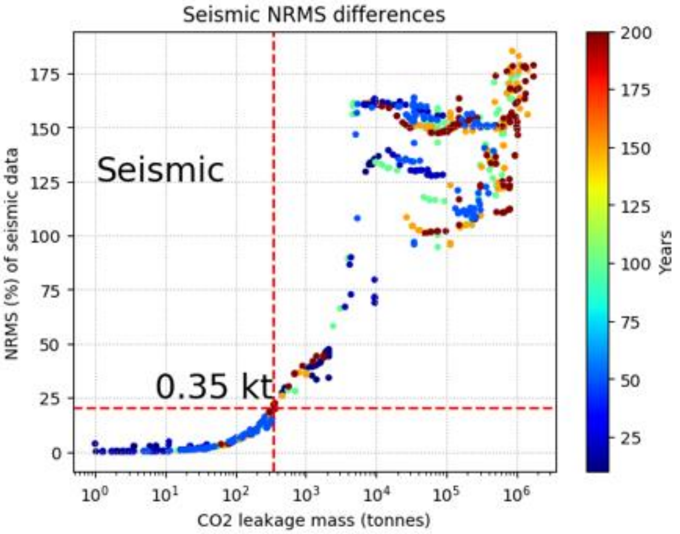

Figure 8: NRMS difference of seismic data as a function of CO_2 leakage mass. Colors represent time steps.

Additionally, 3D seismic data were generated over 4×2 km area using 400 aquifer datasets. A vertical force vector source was placed at the center of the survey area surface. The source wavelet was a Ricker wavelet with a center frequency of 25 Hz. Numerical modeling of elastic-wave propagation was conducted for a total duration of 3 s with a 0.75 ms sampling interval. In a similar way to the 2D case, the NRMS differences between leakage stages and the initial stage were computed for each of the 2,211 seismic traces using the vertical component of seismic data. The maximum NRMS value from all the seismic traces was picked and used as an indicator of leakage detection. The detection threshold of the NRMS change was set to 0.10. Figure 9 shows the normalized NRMS changes as a function of cumulative CO_2 mass leaked and color-coded to the depth of the plume centroid. A clear break point is observed in signal strength once the amount of CO_2 leaked into the aquifer exceeds 20,000 tonnes, defining a reasonable detection threshold for this study.

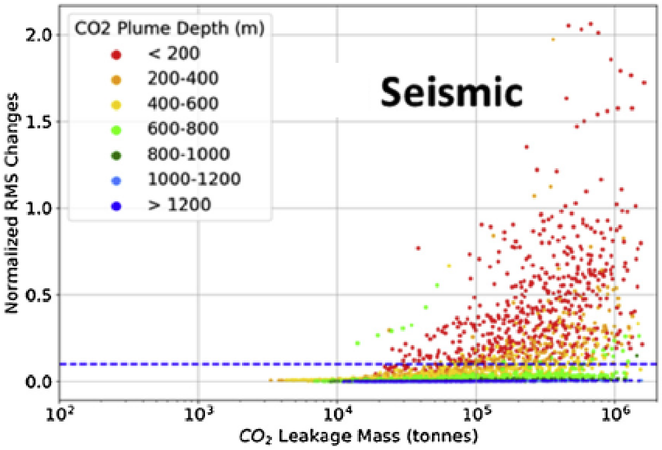

Figure 9: NRMS difference in seismic data as a function of cumulative CO_2 leakage mass. Colors represent different depth intervals.

A small sub-set of these models with a minimum CO_2 plume volume at three depths (i.e., 1,400 m, 667 m, and 34 m) was used to construct synthetic leakage cases with varying CO_2 saturations. Due to the relatively coarse grid used in the flow simulations, the minimum CO_2 plume volume is still quite large. In these simulations, a 2D surface seismic line with a source separation of 50 m and a receiver separation of 30 m was used. The dominant frequency of the source wavelet (Ricker) was 30 Hz. The same sequence of seismic processing steps as above was applied here. The maximum amplitude change and the maximum NRMS from the post-stack migrated seismic data were calculated. Assuming a detection threshold of the maximum amplitude change of 50%, the minimum plume volume detectable at a depth of 1,400 m is 2.32×105 m^3 if the CO_2 saturation is larger than 10% using the seismic acquisition geometry described above. Figure 10 illustrates that the seismic method is sensitive to small CO_2 saturations. However, small or deep CO_2 plumes are below or around the detection threshold, and hence would be difficult to detect in field conditions. Large and shallow CO_2 plumes are detectable with this survey configuration and analysis.

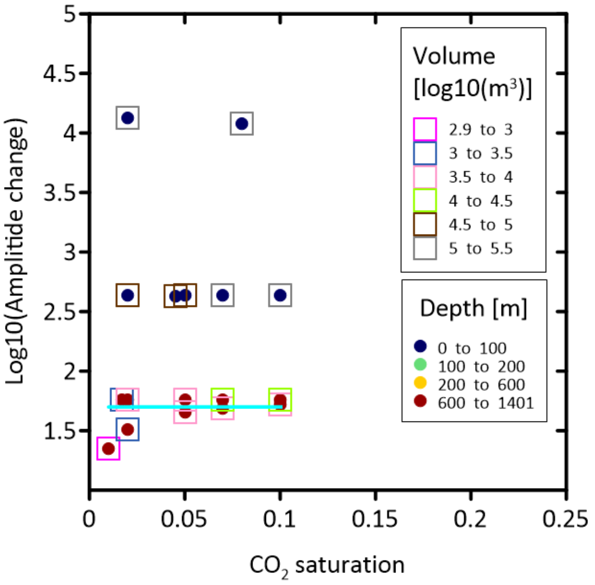

Figure 10: Amplitude change plotted as a function of CO_2 saturation. Colors and symbols illustrate the relationship with the depth and size of the plume. Detection threshold is shown by magenta line.

Scenario 4

The last set of synthetic model scenarios is also based on a hypothetical, commercial-scale GCS model at the Kimberlina site in the southern San Joaquin Basin, California. In this model, referred to as the Kimberlina 2 model, the hypothetical injection well is ~3 km away from a steeply dipping fault. CO_2 is injected at a rate of 2.5 Mt/year for a period of 60 years. Under buoyancy, the primary CO_2 plume develops up-dip in the storage reservoir and along the fault that is a hydraulic barrier laterally, even after CO_2 injection stops. It takes ~40 years for CO_2 in the reservoir to reach the fault, and then it migrates along the fault up-dip to southeast. At an arbitrary time after the end of the injection, changes in the fault permeability through leaky windows (high-permeability zones) are introduced to allow for a migration of CO_2 from the reservoir to secondary formations above the reservoir. The deepest secondary formation is the

Olcese formation, lying between 1,100 and 1,600 m (due to steeply dipping strata). The middle one, the Santa Margarita formation, lies between 600 and 1,200 m and the shallowest formation, the Etchegoin formation, is located between 200 and 500 m below the ground surface. The secondary plumes are under supercritical CO_2 conditions in the lower two zones and under gas CO_2 conditions in the uppermost zone. Modeling scenarios include the secondary CO_2 plume in one of these three formations or in all of them simultaneously. These models are used to evaluate the capability of geophysical techniques, surface seismic among them, to detect small and deep CO_2 plumes in a complex geology.

3D seismic data were generated over a 6×5 km area using a typical commercial survey geometry, with a 30-m in-line source-receiver interval, 250-m source line, and 200-m receiver line separations. The source wavelet was a 20 Hz Ricker wavelet, and three-component data were simulated to 6.2 s using a high-order, finite-difference, elastic-wave modeling algorithm. A 2D line through the leaky location along the W-E direction was extracted and used for least-squares elastic reverse-time migration (LSRTM), which inverts for the images of P- and S-wave velocities and density by minimizing the waveform difference between the synthetic and predicted data. The differences were calculated between models with CO_2 plume and baseline conditions (no CO_2 plume). An example of such difference is shown in Figure 11, where the normalized difference in P-wave velocity image is shown in Figure 11a and the percent difference in the true P-wave velocity model is shown in Figure 11b. The estimated location of the secondary plume agrees very well with the true model. These results illustrate the ability of detecting deep CO_2 plumes using surface seismic. Similar results were obtained for shallower plumes and for models with multiple plumes.

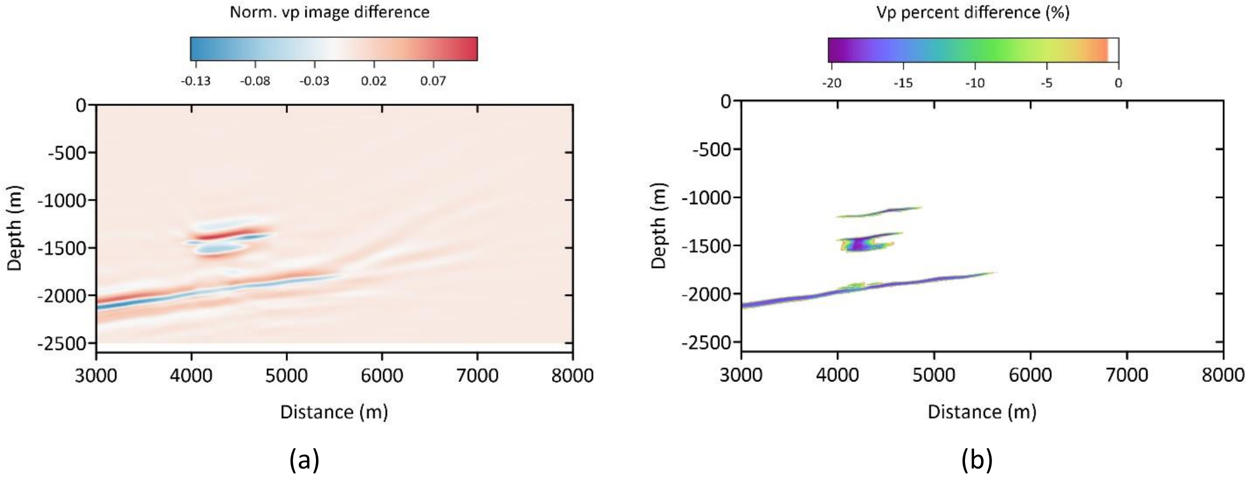

Figure 11: (a) Normalized P-wave velocity image difference and (b) true model difference for a small CO_2 plume at 1,500-m depth demonstrate a great agreement and powerful tool for CO_2 plume detection.

Besides P-wave velocity, it is important to measure other elastic rock properties like S-wave velocities/impedances and density from seismic data for CO_2 monitoring (Clochard et al., 2018). Seismic inversion of P-wave to P-wave reflections (PP component data) gives accurate P-wave impedance. However, it usually gives inaccurate S-wave impedance, and is not capable of estimating the density (Lebrun et al., 2001; Garotta et al., 2002). The emergence of multi-component seismic technologies provides more information to recover elastic rock properties than PP data (e.g., Hardage et al., 2011). Many researchers have used multi-component data like converted P-wave to S-wave (PS) (Van Dok and Gaiser, 2001; Dariu et al., 2003; Barnola and Ibram, 2014) for better estimation of S-wave impedance and density. Figure 12 shows the inverted 2D images of P-wave velocity and density for detecting multiple CO_2 plumes with multi-component data generated by explosive sources for a 2D slice of the Kimberlina 2 model. The image of S-wave velocity is not shown because the changes in S-wave velocity are very small. The estimated P-wave-velocity image agrees quite well with the true one even though the image contains some artifacts. The density image does not agree well with the true density for the deep CO_2 plumes.

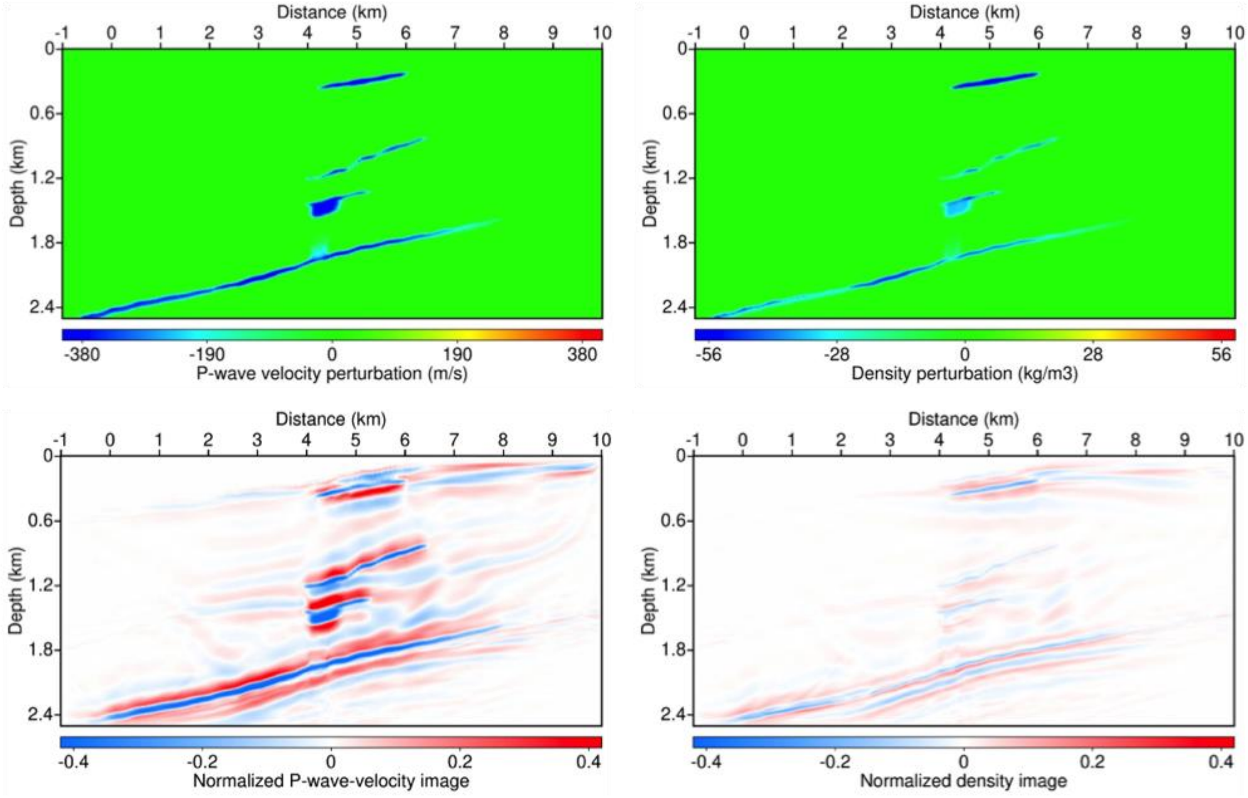

Figure 12: True (top left) and normalized inverted (bottom left) P-wave velocity image difference, true (top right) and normalized inverted (bottom right) density image difference, obtained using explosive sources for a 2D slice of the Kimberlina 2 model.

If a multi-component source with vertical and horizontal components is used, it generates strong shear wave (SS) data, which is very useful for subsurface imaging and monitoring because the data would contain stronger pure SS response than converted PS waves from the target reservoir (Singh and Davis, 2011; Singh et al., 2015). Researchers have used seismic data generated by multi-component sources to provide reliable estimate of S-wave impedance and even density (Singh et al., 2015; Butler et al., 2016; Li et al., 2017). Inverting all multi-component data from multi-component sources has proved capable of providing a reliable Earth model to determine lithology and fluid contents for reservoir characterization, as shown in Figure 13 for the Big Sky CO_2 storage project (Clochard et al., 2018).

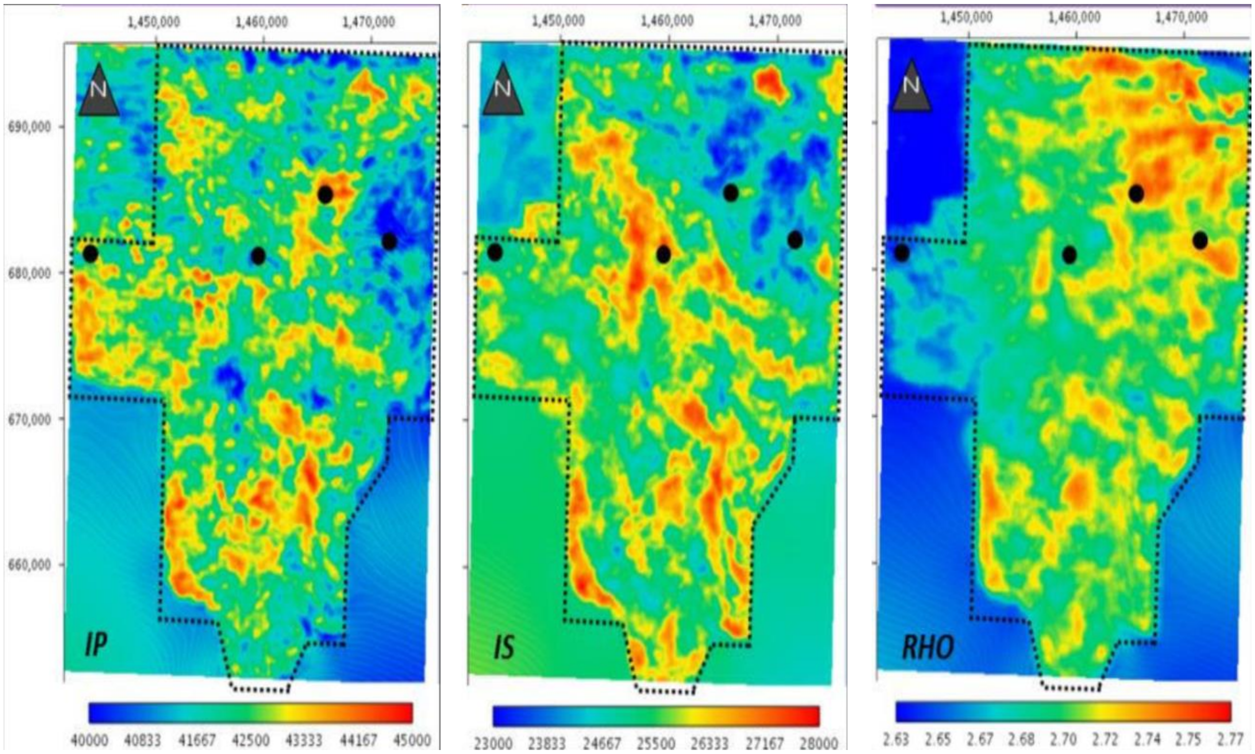

Figure 13: Examples of inverted P-wave impedance (left), S-wave impedance (middle), and density (right) from a 9-component 3D dataset in northern Montana. Figure from Clochard et al. (2018).

Figure 14 further shows inverted 2D images of P-wave velocity and density for detecting multiple CO_2 plumes with multi-component data generated by vertical sources for the 2D slice of the Kimberlina 2 model. The elastic LSRTM method, which simultaneously utilizes PP, PS, and SS components is used for inverting the recorded data. The P-wave-velocity image contains fewer artifacts than the one obtained with explosive sources, and the density image agrees well with the true density model for all CO_2 plumes. The result illustrates the ability to locate the CO_2 plumes at different depths using multi-component seismic data and multi-component sources.

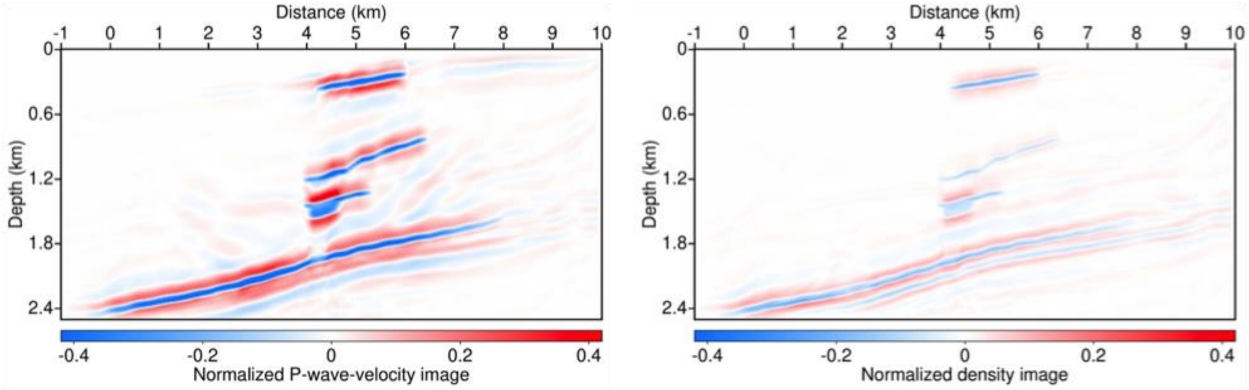

Figure 14: Normalized inverted P-wave velocity image difference (left) and density image difference (right) obtained using multi-component data and vertical sources for a 2D slice of the Kimberlina 2 model.

Presented results and various model scenarios underlay the importance of the appropriate model resolution and survey configuration for detection of CO_2 plume size of interest when evaluating possible monitoring designs.

3. MONITORING USING VERTICAL SEISMIC PROFILING

3.1 BACKGROUND

A vertical seismic profile (VSP) uses subsurface sensors, i.e. sensors deployed in one or more boreholes, along with a seismic source that is typically on the surface, to record seismic waves as they propagate in the subsurface. Because of the subsurface sensors, a VSP will typically have increased spatial resolution, and improved wavefield interpretation and imaging, as compared to surface seismic. However, a VSP image is limited to the region around the borehole (typically a radius of about half of the borehole depth), and therefore, VSP is almost always used in conjunction with surface seismic. In fact, one of the key uses of VSP is to "tie" the seismic response observed in surface seismic to "true" depth as measured in the borehole and thus tying seismic response to formations and rock properties as measured from other borehole tools. VSP usage has been common since the 1980s with many articles and books summarizing the technology (e.g., Galperin, 1985; Balch and Lee, 1984; Hardage, 1983). The term "vertical" originates from the assumption of a vertical borehole (well) and a source near the well, with the recorded waves thus propagating vertically up and down in the earth. However, modern use of the technology spans many experimental geometries which are decidedly not vertical. The term offset VSP (OVSP) is often used for sources offset from the well. Typically, a VSP will be designed specifically to project needs. Figure 15 shows examples of VSP geometries. If sources are used at multiple azimuths for multiple offsets a full volumetric cube of data termed a 3D-VSP can be generated.

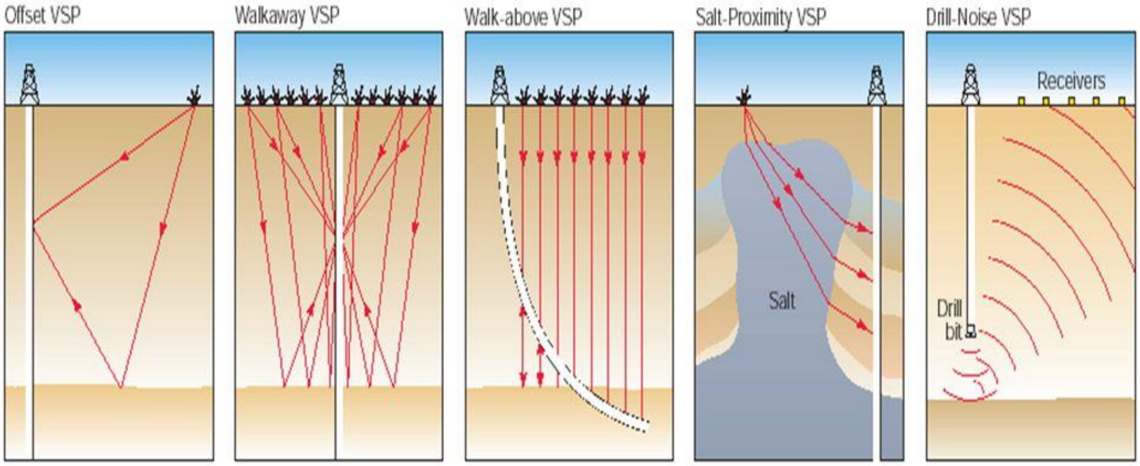

Figure 15: Examples of VSP acquisition geometries: (left to right): Offset VSP involves a source offset from the well such that the raypath is not vertical; Walkaway VSP uses multiple source points typically forming a 2D line through the well; Walk above VSP uses sensors in a deviated well to record a series of near vertical raypaths; Salt-proximity VSP uses a source and sensor geometry that has raypaths passing through a salt dome; Drill-noise VSP is a type of "reverse" VSP with sensors on the surface and the source in the borehole – in this case the source is the drill bit "noise". Figure from Schlumberger (2020).

3.2 CO_2 MONITORING APPLICATIONS

Application of VSP to CO_2 monitoring was originally for CO_2 enhanced oil recovery (EOR), which began at large scale in the early 1970s in the Permian Basin. By the late 1980s, the rock physics basis for seismic monitoring of CO_2 in subsurface reservoirs was established (e.g., Nur and Wang, 1987), and by the late 1990s successful seismic monitoring of injected CO_2 was reported (e.g., Wang et al., 1998). With the initiation of CO_2 storage projects in the 1990s and early 2000s, time-lapse seismic became a primary monitoring tool (see Davis et al. (2019) for a recent review), and VSP became an important subset of seismic monitoring where boreholes were available. While availability of boreholes is standard in EOR applications (since oil production requires wells), CO_2 storage does not require boreholes other than an injection well. In particular, offshore storage may only have an injection well due to the high cost of offshore drilling and maintenance. An example is the long-running Sleipner storage project in Norway, which only has one well, the CO_2 injector. However, the majority of initial CO_2 storage pilot projects have been on land and they have included dedicated monitoring wells. Thus there are already a number of examples of VSP used for monitoring CO_2; a partial list includes the Frio Project (Daley et al., 2008), the Weyburn project (Ahamadi, 2016), the Cranfield project (Hovorka et al., 2011; Daley et al., 2014), the Ketzin project (Gotz et al., 2014), the Otway project (Pevzner et al., 2017), the Decatur project (Coueslan et al., 2013; Bauer et al., 2019), and the Shenhua project (Diao et al., 2020). These and other projects have contributed to the current understanding of the use of VSP to assess (both qualitatively and quantitatively) CO_2 in the subsurface.

3.3 DETECTION AND QUANTIFICATION OF CO_2 FROM VSP SURVEYS

Initial use of VSP, like other seismic monitoring, was for qualitative detection—the identification of CO_2 present in the subsurface with some spatial delineation of the CO_2 plume. This is qualitative in the sense that there is no estimate of saturation and/or mass. Further analysis, using rock physics, allows quantitative assessment of the CO_2 saturation and mass in a given rock volume. The rock physics used to interpret the seismic response to CO_2 typically uses simplifying assumptions (e.g., Daley, 2019) and therefore is subject to error. Nonetheless, geoscientists continue to improve the quantitative assessment of CO_2 saturation from seismic data in general and VSP specifically.

An early example of qualitative VSP monitoring is shown in Figure 16, taken from the Frio project. In this example, a relatively thin plume (~10 m thick), and small total mass (~1,600 tonnes of CO_2) was easily detected due to a relatively large change in velocity (>10%) and the use of the injection well for the VSP sensors (Daley et al., 2008). While this study included a quantitative interpretation of CO_2 saturation calculated from a time-lapse cross-well seismic measurement, the VSP was not interpreted quantitatively. A second Frio injection of ~600 tonnes in a separate reservoir was also detected by a repeat VSP at the same location (Nazari and Daley, 2013).

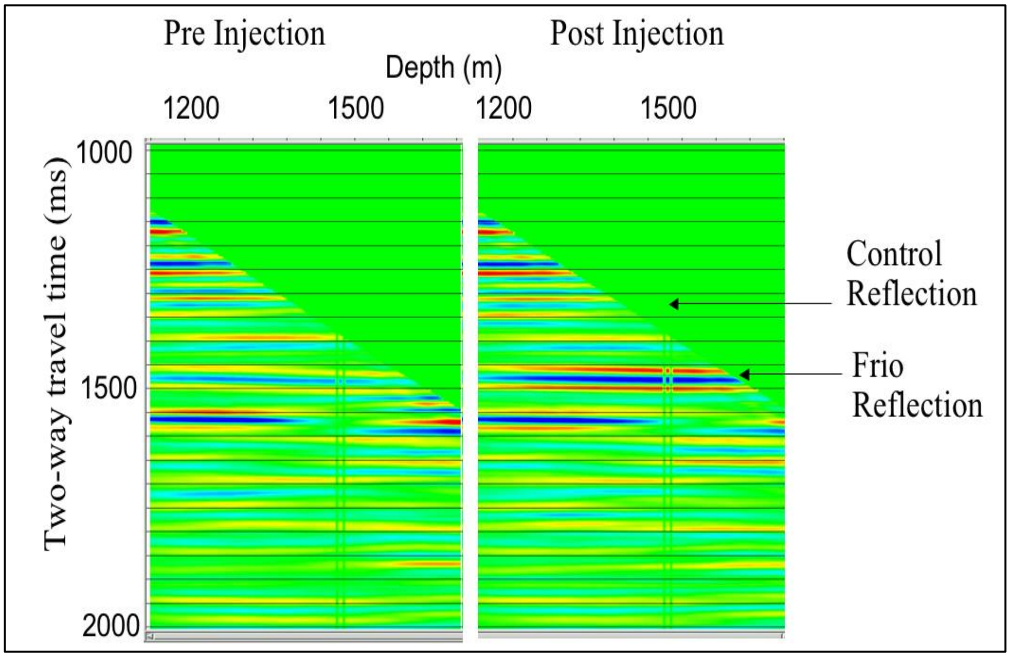

Figure 16: Time-lapse change in observed seismic reflection amplitude from the Frio project. Sensor depth is on the horizontal axis. A large increase in amplitude is observed for the Frio formation which had about 1,600 tonnes of CO_2 injected. The control reflection is the one used for amplitude normalization between surveys. Figure from Daley et al. (2008).

In the Ketzin project, a time-lapse VSP was able to qualitatively identify and map a CO_2 injection of 22,000 to 25,000 tonnes and estimate the seismic velocity change (Gotz et al., 2014). Ivanova et al. (2012) performed a quantitative analysis of the surface seismic data and obtained estimates of mass in place similar to the injection total, albeit with a somewhat arbitrary choice of parameterization.

The Aquistore project provides another example of qualitative monitoring. Changes in 3D-VSP reflections initially imaged 36,000 tonnes injected at over 3-km depth (White, 2019; Harris et al., 2017) and plume imaging continues to date with repeated monitoring (White, 2020). Figure 17 shows the Aquistore 3D-VSP results for 36,000 and 102,000 tonnes injected (White et al., 2018) with the CO_2 plume delineated from change in VSP reflection amplitude calculated as the parameter nRMS in a time window (Landro, 1999).

The measure of nRMS is a standard calculation for qualitative interpretation of VSP (and surface seismic) data (Krah and Christe, 2002). It is a measurement of time-lapse repeatability that does not require supplementary data on rock properties or a rock physics model of seismic response.

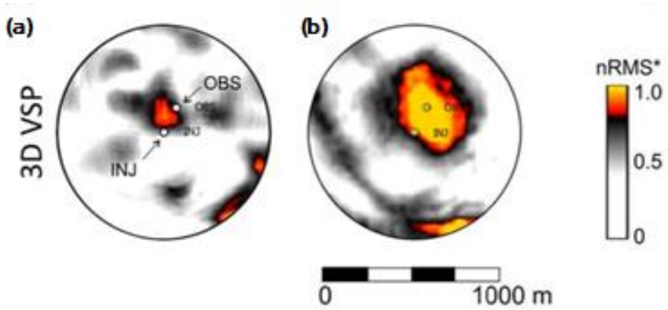

Figure 17: Horizontal slice of VSP reflection change (nRMS) within the Deadwood reservoir level (Aquistore) for 3D-VSP at CO_2 injection amounts of (a) 36,000 and (b) 102,000 tonnes, respectively. The VSP image is a composite constructed from M1-baseline and M2-M1 differences. (Figure modified from White et al. (2018.)

At the Cranfield site, a time-lapse OVSP used NRMS to assess data quality and reflection amplitude change to quantitatively compare measured and modeled response (Daley et al., 2014). The VSP was able to accurately estimate the change in seismic response of the reservoir to CO_2, thus allowing the 4D surface seismic to be more accurately interpreted. Acquisition issues limited the OVSP analysis to the immediate vicinity of the well using a “corridor stack” (Daley et al., 2014), but this approach allowed use of offsets over 1,200 m for the ~3-km deep injection well. Consistent results from multiple offsets added confidence to the interpretation. Figure 18 shows the NRMS and reflection amplitude time-lapse change for the OVSP source points for both the field data and numerically modeled data, respectively. Along with high NRMS, indicating poor time-lapse repeatability due to injection, the data amplitude change matched the modeled response and was able to detect the CO_2 plume. This result could be considered a hybrid of qualitative (NRMS) and quantitative (modeled amplitude change) interpretation.

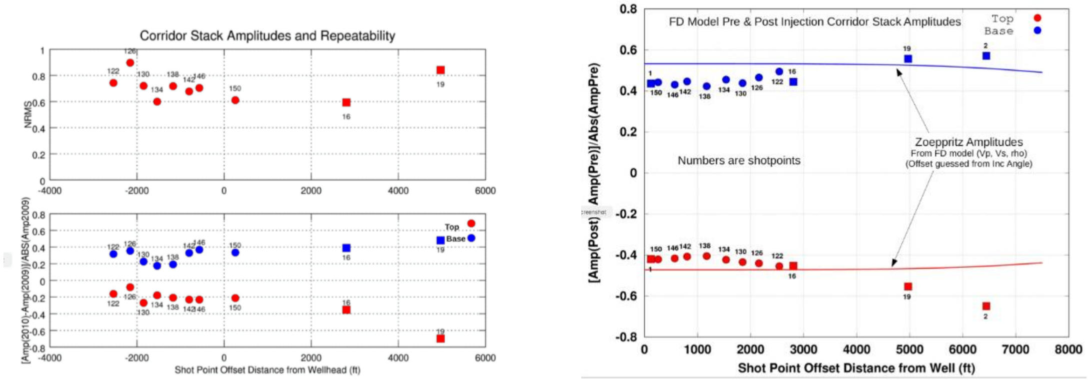

(a) (b)

Figure 18: (a) Interpretation of OVSP data from Cranfield showing (top) NRMS values, and (bottom) change in reflection amplitude for top and base of reservoir; (b) the predicted change in reflection amplitude (both numerical and analytic) for top and base of reservoir. The symbol labels indicate shot point number. Note that (a) sub-plots are calculated from data and have positive and negative offsets. Numerical analysis (b) used finite-difference modeling (symbols) and analytic analysis use Zoeppritz equation calculation (lines) with estimated incidence angles for each offset. The CO_2 induced velocity change used for modeling came from time-lapse crosswell measurement (Daley et al., 2014).

An example of quantitative interpretation of CO_2 saturation is shown in Figure 19 from the Weyburn 3D VSP (Ahamadi, 2016), which shows CO_2 saturation in a horizontal cross section. This result requires rock physics models to convert seismic response to fluid saturation.

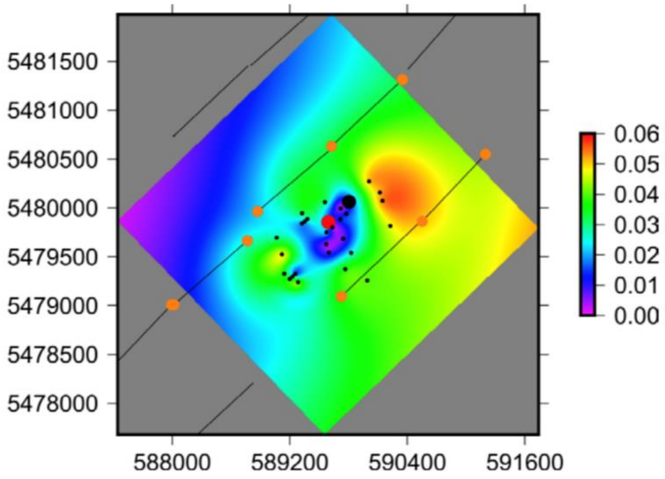

Figure 19: CO_2 saturation values from the Weyburn 3D VSP analysis for a horizontal cross section in the reservoir zone (from Ahamadi, 2016).

3.4 LIMITATIONS ON QUANTITATIVE INTERPRETATION

A recent experiment, designed specifically to test detectability of seismic monitoring, was carried out at the Otway project. The time-lapse monitoring was done following the injection of 5,000, 10,000, and 15,000 tonnes of CO_2 (Pevzner et al., 2017). Popik et al. (2020) were able to detect the plume and track its evolution (Figure 20).

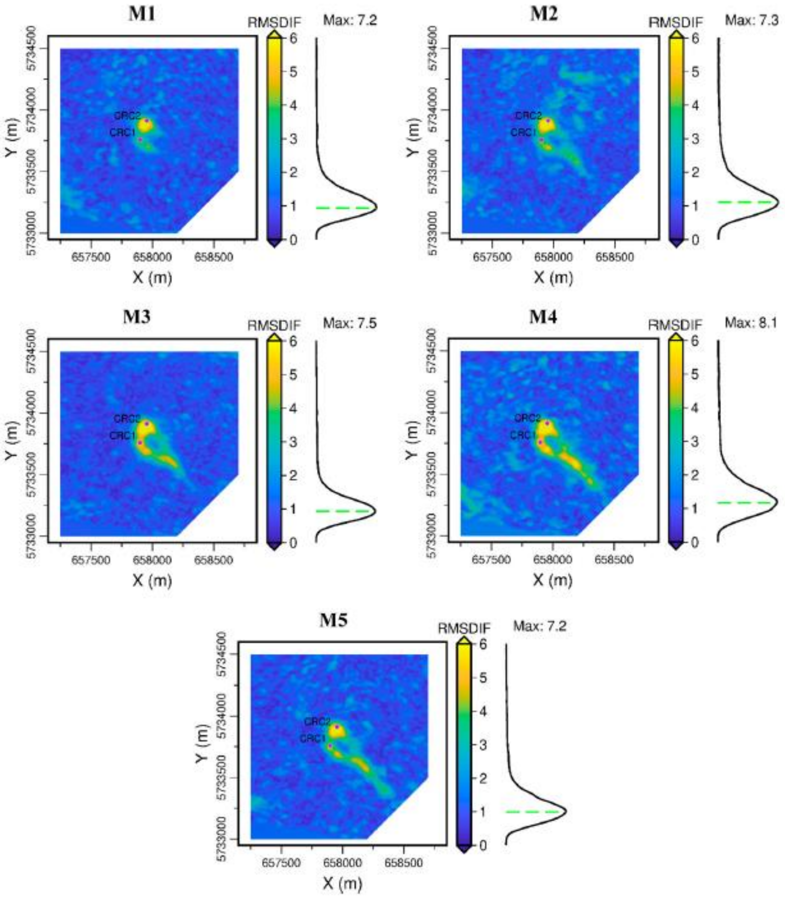

Figure 20: Maps of RMS amplitudes of the time-lapse signal obtained for monitoring surveys M1–M5 in 24 ms time window centered at 1,210 ms (corresponding to the injection interval). The histograms show the distribution of the ambient noise presented on each map. The value "Max" is the maximum amplitude of the time-lapse signal (after normalization) for each monitor. Figure 6 from Popik et al. (2020).

Pevzner et al. (2015) used surface seismic data and numerical modeling to assess quantitative detectability. In Figure 21, Pevzner et al. (2015) showed the tradeoff between effective diameter of a 30 kt CO_2 plume and the detectability from data as measured by the parameter N = rms(signal+noise)/rms(noise). As N increases (increasing data quality), the effective diameter of a detectable plume decreases. Similarly, in Figure 22, Pevzner et al. (2015) showed the effective diameter for plumes of three sizes (10, 15, and 30 kt) versus the detectability parameter N.

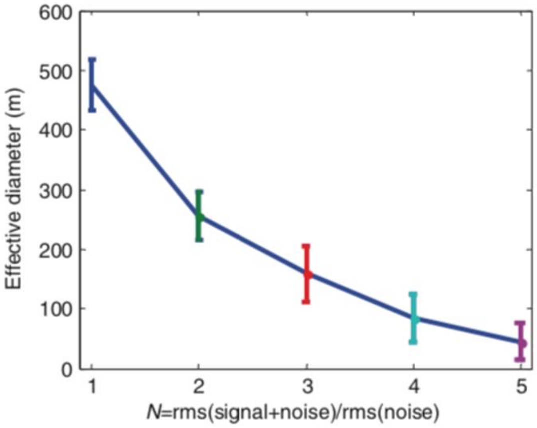

Figure 21: Effective plume diameter detectable for different signal quality cut-offs (as a function of the threshold N) for 30,0000 tonnes of CO_2/CH_4 at Otway Stage 2. (From Pevzner et al., 2015).

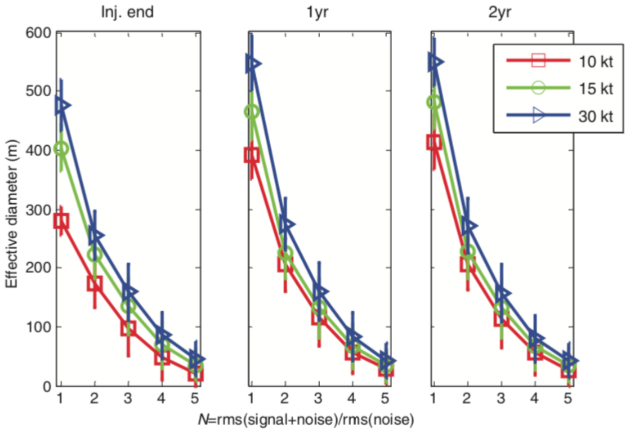

Figure 22: Effective diameter of detectability for injection volumes of 10, 15, and 30 kt as a function of the threshold N (a measure of SNR and detectability). (From Pevzner, et al., 2015)

Pilot tests have had success in qualitative detection and characterization of relatively small amounts of CO_2 with VSP, ranging from the Frio (1,600 tonnes), Otway (5,000–15,000 tonnes) and Ketzin projects (1,600–36,000 tonnes), to Aquistore (30,000–100,000+ tonnes). Quantitative interpretation, using available data on rock properties and a rock physics model, and often including reservoir models, can be calculated, although typically without uncertainty assessment. However, all projects have some limitations on quantitative interpretation, and many projects use the qualitative results. For example, Diao et al. (2020) reported on VSP monitoring of 130 kt and 250 kt of CO_2 in a multi-layered reservoir and interpret plume distribution; however, they caution "the accuracy and credibility of the 2D VSP seismic technology must be studied further at the Shenhua site with its complicated geology characteristics."

The Shenhua case is one example of difficulties from the many factors impacting the utility of VSP for monitoring. Problems include variability in data acquisition, both within a single survey and between time-lapse surveys (another example is the Cranfield VSP in Daley et al., 2014). Repeatability of the data acquisition may be the single most important factor in VSP monitoring.

High-quality time-lapse projects often utilize permanent sensors, such as at Aquistore, Otway, and Ketzin. For VSPs, the emerging technology of distributed acoustic sensing (DAS), which is fiber optic-based sensing, has great promise for enabling permanent deployment of sensors in boreholes. DAS currently has lower sensitivity than conventional borehole sensors (e.g., clamping geophones or accelerometers), when comparing a single DAS channel with a single geophone channel; however, this limitation can be addressed with increased source effort (e.g., Daley et al., 2016). Since DAS allows all the sensors in the well to be acquired simultaneously, increasing the source effort is economically viable. An important consideration in DAS VSP is whether a fiber cable is permanent (typically cemented behind casing). The advantages of permanent cable DAS VSP for repeatability and data quality are very compelling, such that any monitoring well should consider cementing fiber in place.

A good early example of DAS VSP for CO_2 monitoring is the Aquistore project, which has fiber permanently emplaced in a monitoring well to 2.7-km depth (Harris et al., 2017), which successfully replaced surveys with conventional borehole geophone sensors. Even with permanent sensors, the source repeatability is a factor that typically reduces time-lapse data quality. Both access to surface locations and consistency of near-surface properties at a given location are typical problems with time-lapse repeats of VSP (and surface seismic).

Recently, the limits of quantitative detection with seismic was explicitly investigated for the Otway Stage 2c test by Glubokovskikh et al. (2020) using an integrated acoustic inversion workflow with statistical detection of plume boundaries. Among their findings is an assessment of the tradeoff between the threshold used for the plume “edge” and falsely detected CO_2. Figure 23 shows this tradeoff using change in acoustic impedance.

Another difficulty in quantitative analysis of VSP data is geologic heterogeneity, a problem which compromises all monitoring techniques. The Shenhua, Ketzin, and Cranfield projects are three examples of geologic heterogeneity hampering quantitative analysis. If properties such as porosity, and matrix mechanical properties are changing at scales of less than a few wavelengths, errors will occur. If the reservoir layers are thin (less than a wavelength), accurate estimates of CO_2 saturation are more difficult. The matrix properties of the reservoir and surrounding layers also impact the accuracy of quantitative seismic interpretation. Pevzner et al. (2015) attempted to assess this for Otway by synthetic analysis of multiple realizations of a reservoir model. Quantitative analysis also relies on the use of a rock physics model to relate seismic change to fluid/gas saturation change, and there are notable variations between rock physics models. Additionally, geochemical alteration of the rock matrix can significantly affect the seismic response, masking the effect of changing CO_2 saturation, and this is rarely accounted for in rock physics models and seismic analysis.

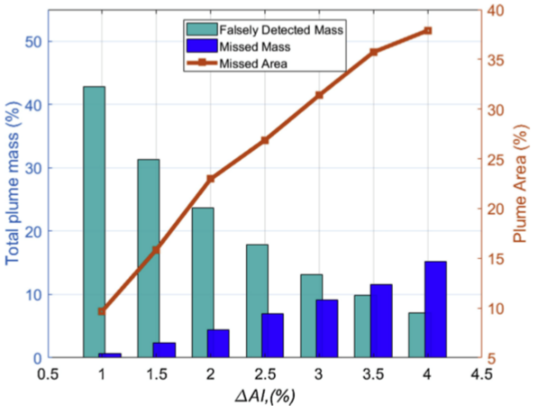

Figure 23: Total plume mass, either falsely detected or not detected, vs. seismic response (change in acoustic impedance) shown as a bar graph, along with plume area missed (not detected) vs. acoustic impedance change. (From Glubokovskikh et al., 2020).

4. GRAVITY MONITORING

4.1 BACKGROUND

The gravity method is a non-invasive geophysical technique that measures differences in the downward acceleration of gravity at a series of specific locations. When CO_2 is injected into a porous formation, the original fluid within the pores of the rock matrix is progressively replaced or mixed with the CO_2. Because the density of the injected CO_2 is less than that of the original fluid (e.g., brine) (Figure 24), CO_2 injection will induce a bulk density decrease. The changes in density over time will induce perturbations—referred to as anomalies—in the measured local gravitational field. Depending on the situation, these gravity anomalies may be measured using gravimeters at the surface or in a borehole. Single-epoch gravity surveys (e.g., site characterization) provide absolute density values and density distribution in the subsurface. Time-lapse or 4D surveys measure the density change over time. Early successful time-lapse applications include monitoring hydrocarbon production (e.g., in the Prudhoe Bay field in Alaska, USA) using water flooding in EOR operations (Ferguson et al., 2008; Hare et al., 1999).

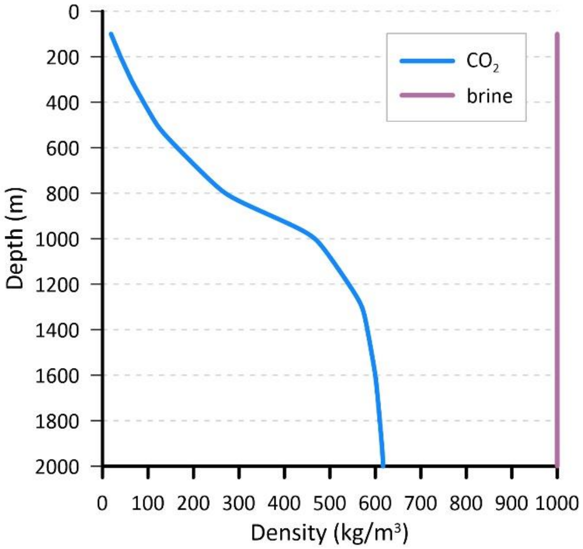

Figure 24: Change in density as a function of depth.

To quantify gravity changes over time, the total wet-bulk density ($\rho_{\text{wet bulk}}$) of a given volume for a specific time step must be determined. Wet-bulk density ($\rho_{\text{wet bulk}}$) is generally considered to be the density of the rock matrix that takes into account the density of the solid matrix (rock) ρ_{rock}, and the density of the brine fluids contained in the pore space ρ_{w}. As the original fluid contained in the pore space is replaced by CO_2, $\rho_{\text{wet bulk}}$ can be expressed as

$$\rho_{\text{wet bulk}} = (1 - \phi)\rho_{\text{rock}} + S_{\text{w}}\phi\rho_{\text{w}} + S_{\text{CO}_2}\phi\rho_{\text{CO}_2} \tag{1}$$

where ρ_{CO_2} is the CO_2 density, ϕ is the porosity, S_w is the brine saturation, S_{CO_2} is CO_2 saturation (any phase), and $S_w + S_{CO_2} = 1$. The wet bulk density change, $\Delta\rho$, associated with the CO_2 injection can be expressed as (Eiken et al., 2008; Jacob et al., 2016):

$$\Delta\rho = \Delta S_{CO_2}\phi\ (\rho_{CO_2} - \rho_w) \qquad (2)$$

where ΔS_{CO_2} is the change in CO_2 saturation.

In typical carbon capture and sequestration (CCS) operations, CO_2 is injected at pressure and temperature conditions such that it reaches supercritical conditions or is less dense and more compressible than the brine. On the other hand, CO_2 in shallow depths is in a gas phase and occupies much larger volume. The gravity signal is directly proportional to changes in bulk density.

4.2 SURFACE GRAVITY

Synthetic models were used in evaluating sensitivities or detection capabilities of surface gravity to detect CO_2 plume at different depths. A conceptual model assumes that CO_2 moves out from the storage reservoir, accumulates in a secondary trap above the storage horizon, and forms a cylinder-shaped plume. Kimberlina 2 model parameters were used to calculate CO_2 density (Appriou et al., 2020). A hydrostatic pore pressure gradient of 10.5 kPa/m, a geothermal temperature gradient of 26.8°C/km, with a surface temperature of 21.8°C, and porosity of 25% were used. The cylinder height was 20 m, the radius varied from 500 to 3,000 m, and CO_2 saturations between 5 and 60% were considered.

Figure 25 shows CO_2 saturation (a, c, e) and CO_2 mass (b, d, f) as functions of depth for a variable cylinder radius. Figures 25a and 25b shows these relationships for the detection threshold of 4 μGal, Figures 25c and 25d for 7 μGal, and Figures 25e and 25f for 10 μGal. These figures can be used to determine quickly in which conditions a secondary plume can be detected by a surface gravity survey at a site with a similar characteristic as described above. For example, they clearly show that the size (radius) of the plume controls the depth at which this plume would be detectable for a given CO_2 mass and a given detection threshold. An increase in the plume radius or CO_2 saturation increases the depth of a detectable plume. The CO_2 mass increases with plume size and depth. For example, in Figure 25a, a plume of 500-m radius and 20% CO_2 saturation would be detectable to 800-m depth, while for 1,000-m radius and the same CO_2 saturation the depth would be 1,200 m. Using Figure 25b, for a detection threshold of 4 μGal, a 10 kt CO_2 secondary plume with a radius of 500 m can be detected at a depth of 300 m, but the plume mass will need to be 1,000 kt to be detected at a depth of 1,200 m. If this threshold is set at 10 μGal (Figure 25f) the 10 kt and 1,000 kt CO_2 plumes would only be detected at shallower depths, 200 m and 800 m, respectively.

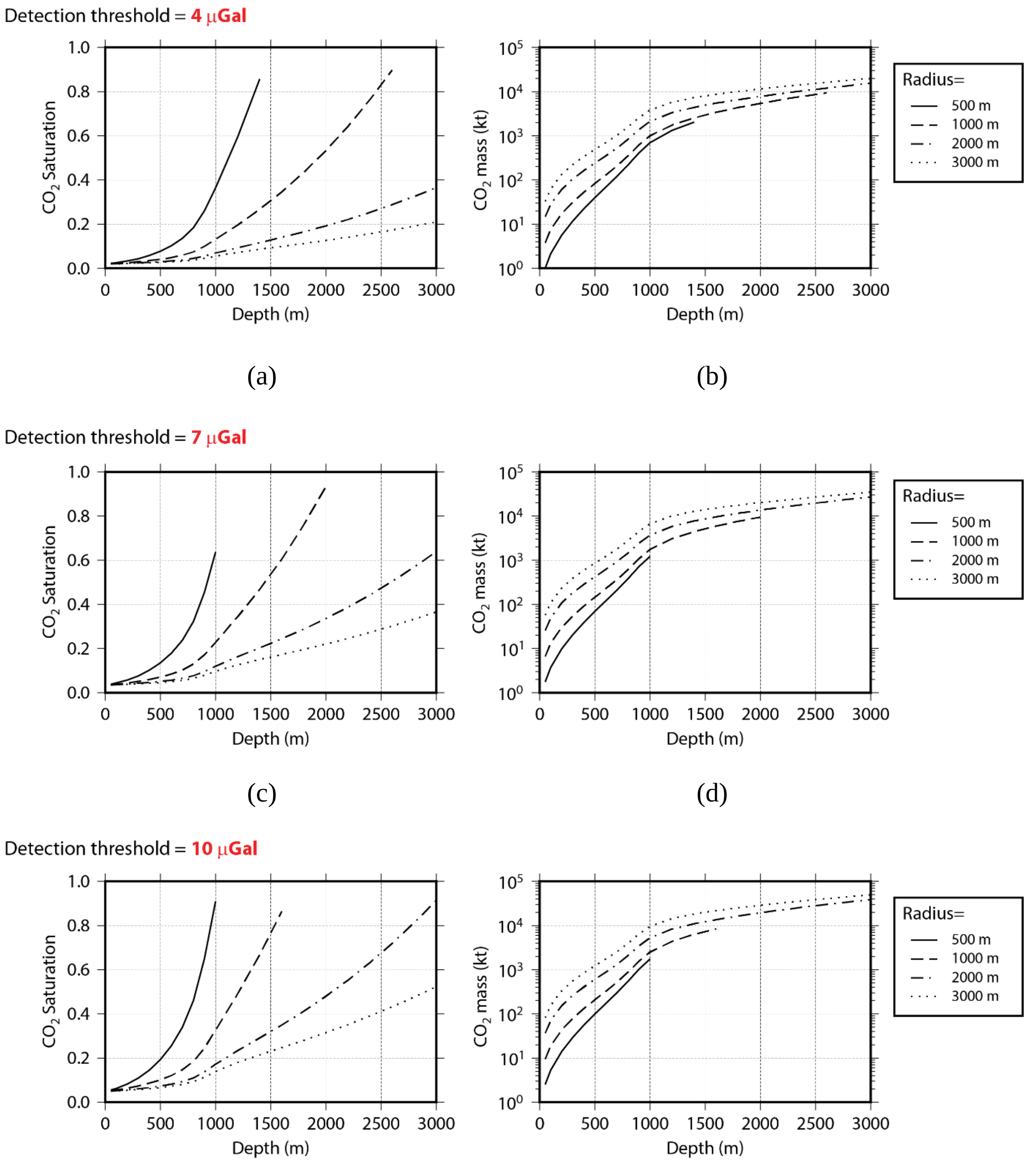

(a) (b)

(c) (d)

(e) (f)

Figure 25: CO_2 saturation (a, c, e), and CO_2 mass (b, d, f) as functions of depth for a variable cylinder radius. The detection threshold is 4 μGal in (a) and (b), 7 μGal in (c) and (d), and 10 μGal in (e) and (f).

Note, that there is an inflexion of all curves around 800 m corresponding to a major change in CO_2 density linked to the transition to supercritical state. It must also be noted that curves tend to an asymptote making difficult to determine the correct CO_2 mass at great depths.

Figure 26 shows the plume radius (a, c, e) and CO_2 mass (b, d, f) as functions of depth for variable CO_2 saturations. Figures 26a and 26b show these relationships for the detection threshold of 4 μGal, Figures 26c and 26d for 7 μGal, and Figures 26e and 26f for 10 μGal. These figures clearly illustrate the relationship that exists between CO_2 saturation and the plume depth and size: the higher the saturation, the greater the depths of detection for a given radius of the CO_2 secondary plume or of a smaller size.

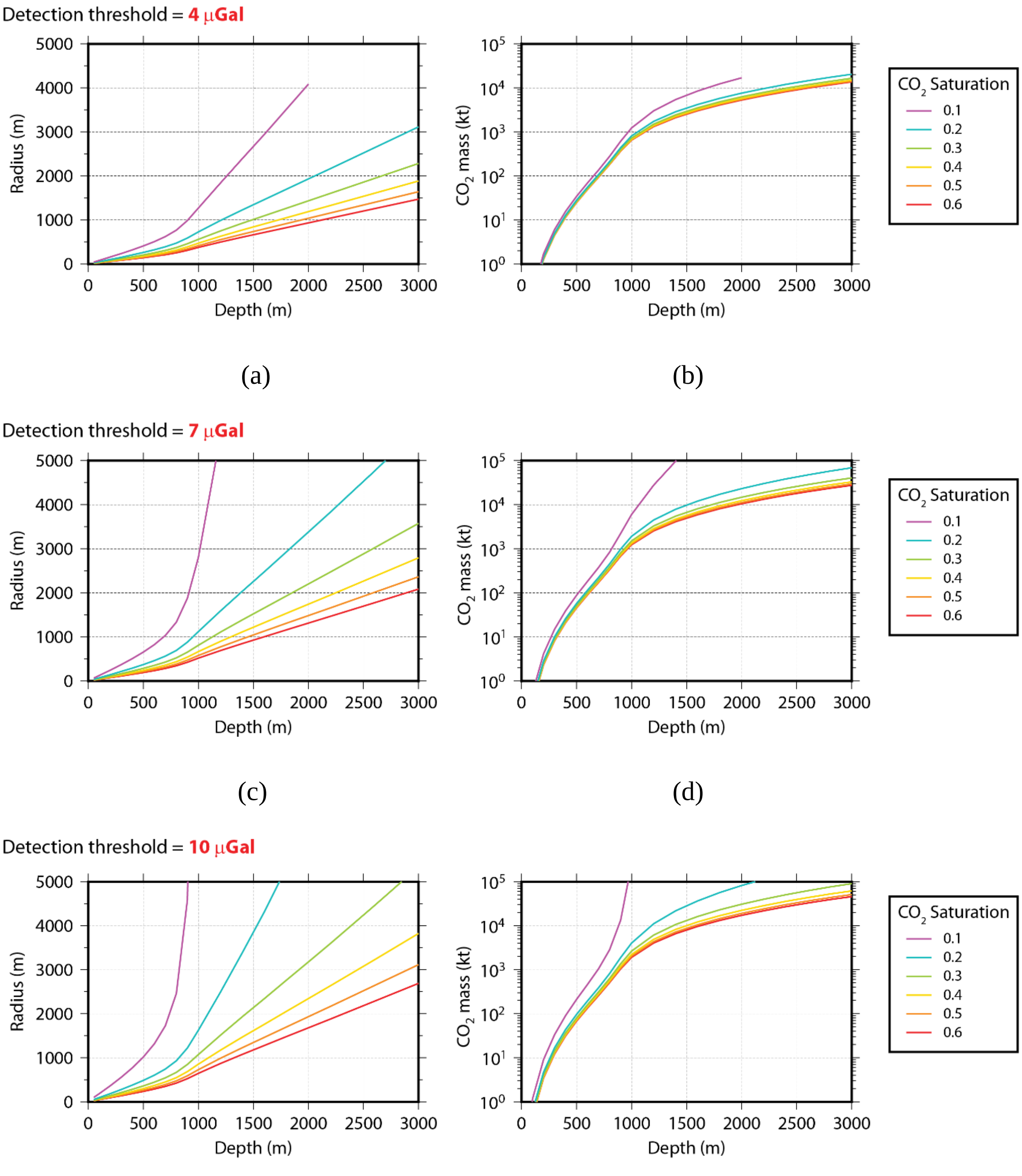

(a) (b)

(c) (d)

(e) (f)

Figure 26: CO_2 plume radius (a, c, e), and CO_2 mass (b, d, f) as functions of depth for a variable CO_2 saturation. The detection threshold is 4 μGal in (a) and (b), 7 μGal in (c) and (d), and 10 μGal in (e) and (f).

In time-lapse gravity monitoring, it is highly desirable that repeated gravity measurements are performed at the same locations. This eliminates a need for typical data processing corrections depending on the location at the surface of the Earth. However, the elevation of the measurement point must be determined carefully each time by local high-precision geodetic surveys or by satellite positioning systems. This determination is needed to detect any deformation of the surface ground that could induce a large gravity anomaly (known as the free-air gravity correction, roughly 0.3086 mGal/m). In addition, other temporal sources of gravity changes such as near-surface hydrological sources should be taken into consideration and separated from the CO_2 injection response.

Earlier numerical studies demonstrated that time-lapse gravity could be successfully applied as a monitoring tool for GCS (Gasperikova and Hoversten, 2008; Jacob et al., 2016; Krahenbuhl et al., 2015). The first deployment of time-lapse gravity surveys at an actual storage site on the sea floor was implemented at the Sleipner site in Norway (Alnes et al., 2011; Alnes et al., 2008; Nooner et al., 2007). The repeated surveys allowed gravity anomalies larger than 10 μGal (1 Gal = 1 cm/s^2) to be detected, and constrained the density of the injected CO_2 and the rate of dissolution. However, the depth of CO_2 injection operations, generally deeper than 800 m, and the error associated with gravity surveys (typically 5 μGal according to Jacob et al. (2010)), limit the performance of surface measurements.

4.3 BOREHOLE GRAVITY

Popta et al. (1990) and Gasperikova and Hoversten (2008) demonstrated that borehole gravity measurements are sensitive to a geological structure of a sufficient density contrast if the distance between the device and the structure is less than one or two times the thickness of the zone of the density contrast. Figure 27 (Figure 6 in Gasperikova and Hoversten, 2008) shows a CO_2 wedge of 250-m radius and density of 2,260 kg/m^3 (representing 20% CO_2 saturation in 20% porosity) inside of a 100-m thick sand layer with a density of 2,285 kg/m^3 at the depth of 1,000 m. The background density is 2,160 kg/m^3. The borehole gravity response as a function of distance from the wedge edge is shown in Figure 28. The maximum response at the edge of the CO_2 wedge is 10 μGal. (due to 1% change in density). The responses decrease with distance away from the wedge: 50 m away from the wedge the response is 6 μGal., 100 m away response decreases to 4.4 μGal., and 200 m away it is down to 2.5 μGal.

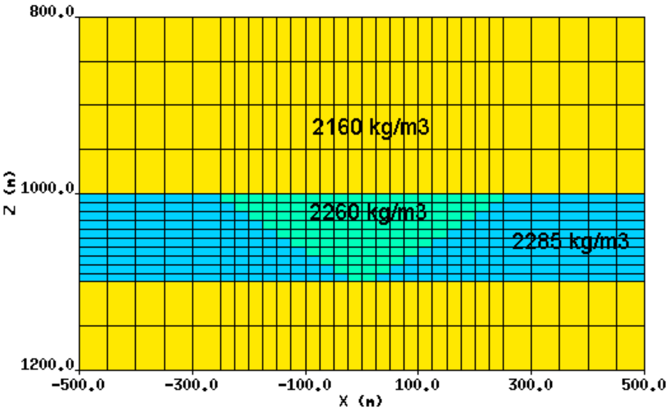

Figure 27: CO_2 wedge model.

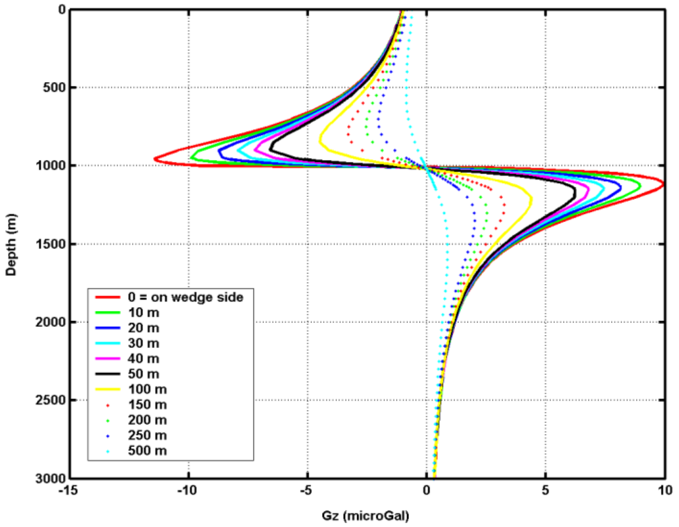

Figure 28: Borehole gravity response of the model in Figure 27a as a function of distance from the wedge edge.

The feasibility of borehole gravity monitoring was also investigated by using a simple prism model (Figure 29) and calculating three-component gravity responses. CO_2 plume was represented by a prism of a constant thickness (20 m) and varying horizontal dimensions based on the CO_2 mass. The density contrast with the host rock varies with depth due to the variation of CO_2 density with depth. Surface temperature of 10°C, hydrostatic pressure gradient of 9.84 MPa/km, geothermal gradient of 25˚C/km, and porosity of 25% were used for all scenarios. Scenarios included five different values of CO_2 mass from 10 to 100 kt, seven different levels of CO_2 saturation from 5% to 50%, and 13 different depths from 50 m to 3,000 m.

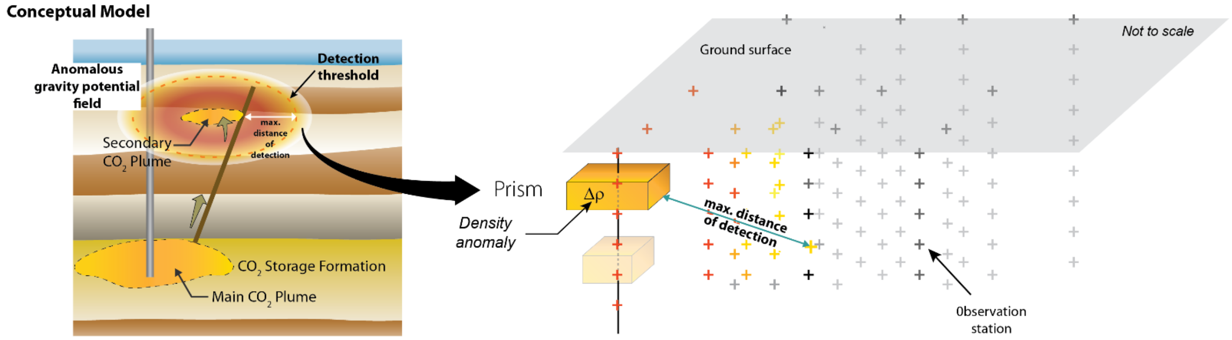

Figure 29: Conceptual model for borehole gravity measurements calculations.

For each depth of the prism top, the hydrostatic pressure is determined using the hydrostatic gradient and the temperature using the geothermal gradient. Then the corresponding CO_2 and water densities at this depth are obtained using the table by Lemmon et al. (2018) and finally the fluid density contrast is obtained by Equation 2.

The center of the prism is located in x=0 and y=0 of a grid, where the gravity field is computed at each node. The dimensions of the grid are 6,250 m in x and y and 3,000 m in z. The spacing of the nodes is constant in z (10 m) and increases by steps in x and y away from the prism (10, 100, and 250 m). Thanks to the symmetry of the problem, only two components g_x and g_z can be computed and only for one quadrant (Figure 30).

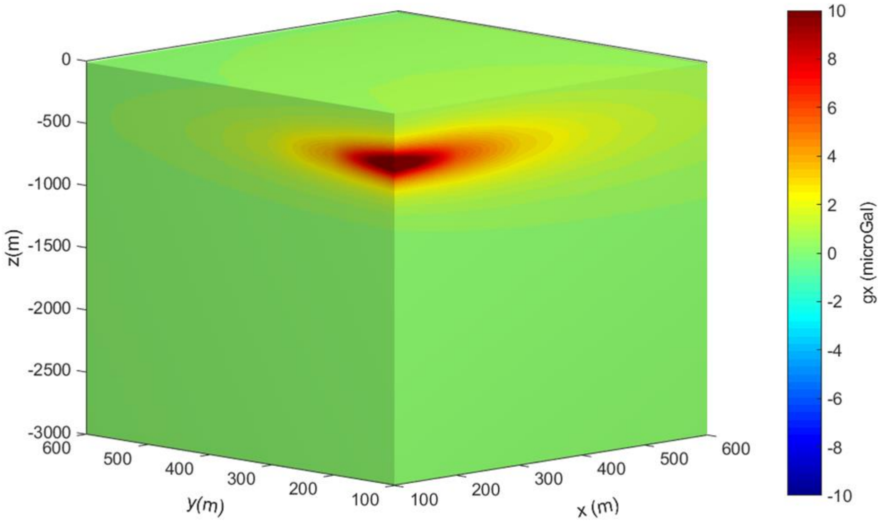

Figure 30: 3D gravity change of the horizontal component g_x induced by 10 kt of CO_2 plume represented by a horizontal prism located in x=0, y=0, and z=410 m and 50% CO_2 saturation.

For each value of the CO_2 mass, CO_2 saturation, and depth of the prism top, the gravity anomalies are computed in each node of the grid using the algorithm proposed by Dubey and Tiwari (2016). Then the maximum distance from the edge of the prism to the node at which one of the components (g_x or g_z) is above a given threshold is determined. The sensitivity of borehole measurements was evaluated for two detection thresholds, 5 and 10 μGal, which are typical detection thresholds currently assumed for borehole measurements. In Figures 31–34, the maximum distance at which a plume can be detected in both horizontal (g_x) and vertical (g_z) components is plotted as a function of depth for seven different CO_2 saturations, two detection thresholds, and six different CO_2 masses.

For deep CO_2 plumes (supercritical conditions), the borehole would have to be located within few tens of meters of the edge of the CO_2 plume to be able to detect it, ranging from 20 to 200 m, depending on the mass of CO_2 and CO_2 saturation. At shallow depths, the detection of plumes becomes easier and can reach up to 1,500 m away for the biggest CO_2 plume.

The mass of the CO_2 plume is fundamental for its detection. As shown in Figure 31 for a detection threshold of 5 μGal, a scenario with 30% CO_2 saturation (green dot), and the CO_2 plume at 200-m depth, the detection distance will range from less than 500 m to about 1000 m, for CO_2 mass of 10 and 100 kt, respectively.

The smaller the detection threshold, the greater the chances of plume detection. While the distance of detection for horizontal component is overall reduced compared to the vertical component, there is still value of considering it, especially for shallower CO_2 plumes. Assuming such measurements will be feasible in the near future, they could clearly add an azimuthal information regarding the location of the plume, which could be of high value.

Borehole gravity surveys applied to GCS have been numerically assessed (Gasperikova and Hoversten, 2008; Krahenbuhl and Li, 2012; Krahenbuhl et al., 2015), but only a limited number of field tests have been undertaken. The most documented study was done for the field test conducted at the Cranfield site, Mississippi (Dodds et al., 2013). That field test yielded results about density changes associated with CO_2 injection in a complex geologic environment.

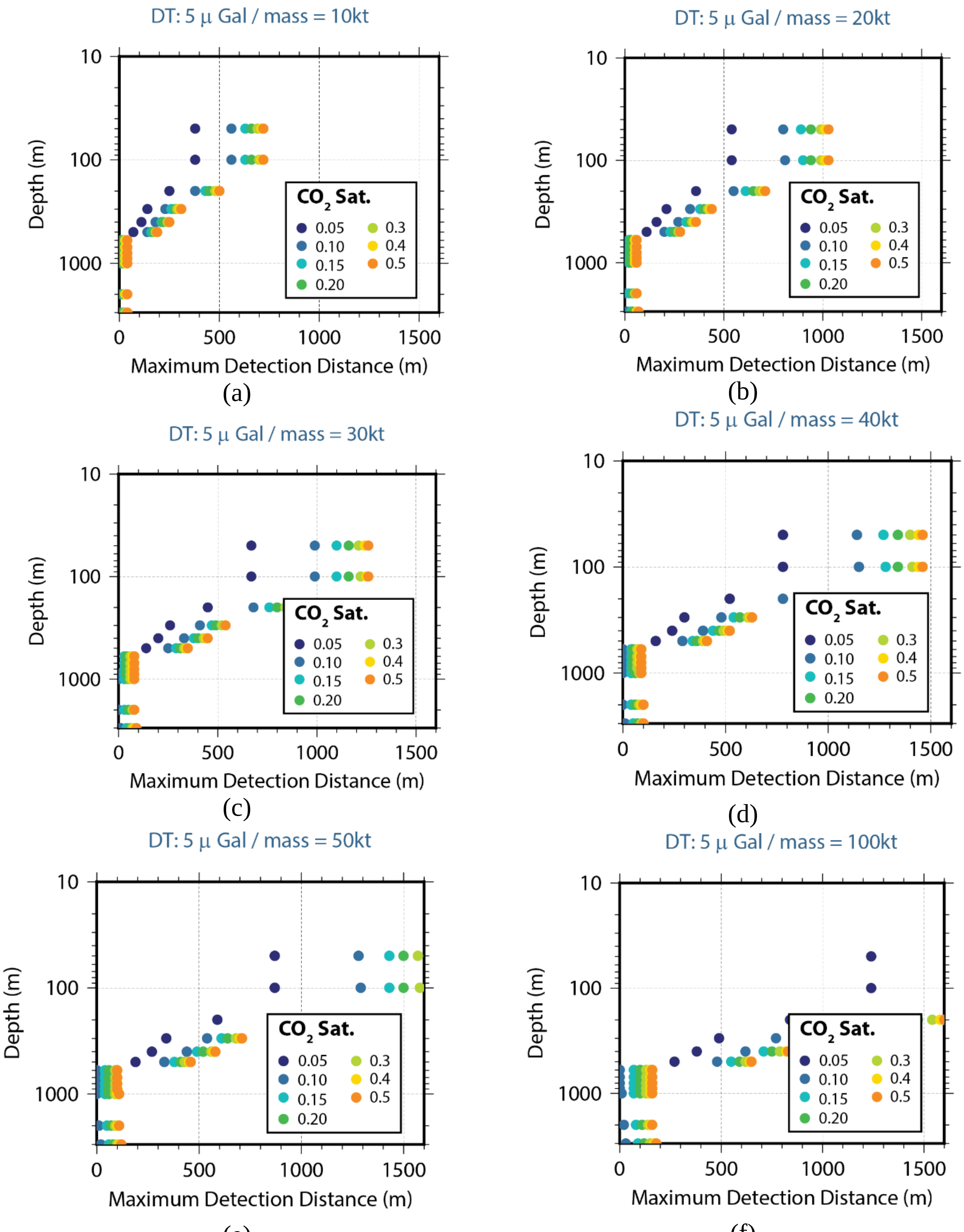

(a) (b) (c) (d) (e) (f)

Figure 31: Maximum distance of detection vs. depth of a 5-µGal change in the vertical gravity component g_z for (a) 10 kt, (b) 20 kt, (c) 30 kt, (d) 40 kt, (e) 50 kt, and (f) 100 kt CO_2 mass and CO_2 saturations varying from 0.05 to 0.5 (5–50%) (colored dots).

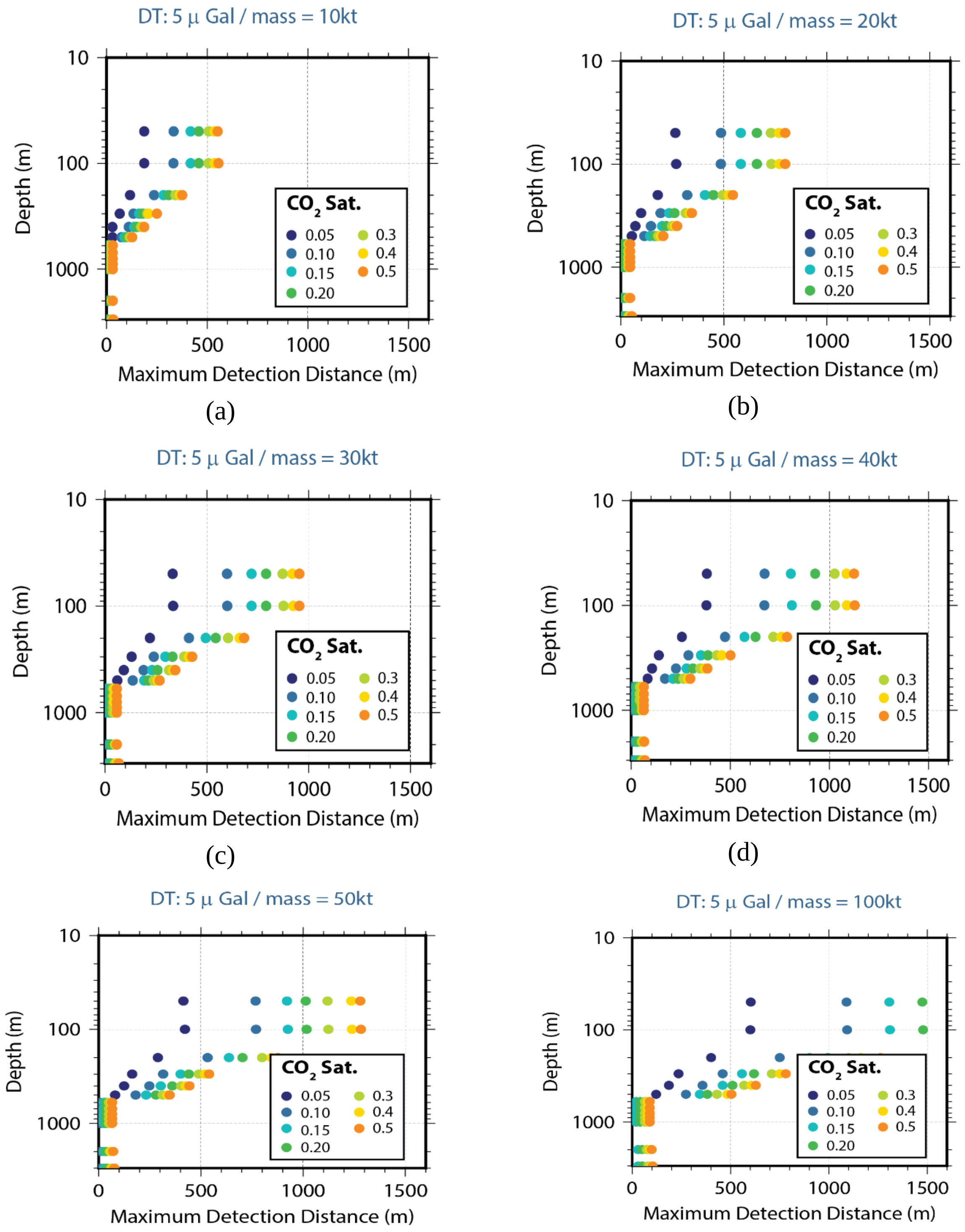

(a) (b) (c) (d) (e) (f)

Figure 32: Maximum distance of detection vs. depth of a 5-μGal change in the horizontal gravity component g_x for (a) 10 kt, (b) 20 kt, (c) 30 kt, (d) 40 kt, (e) 50 kt, and (f) 100 kt CO_2 mass and CO_2 saturations varying from 0.05 to 0.5 (5–50%) (colored dots).

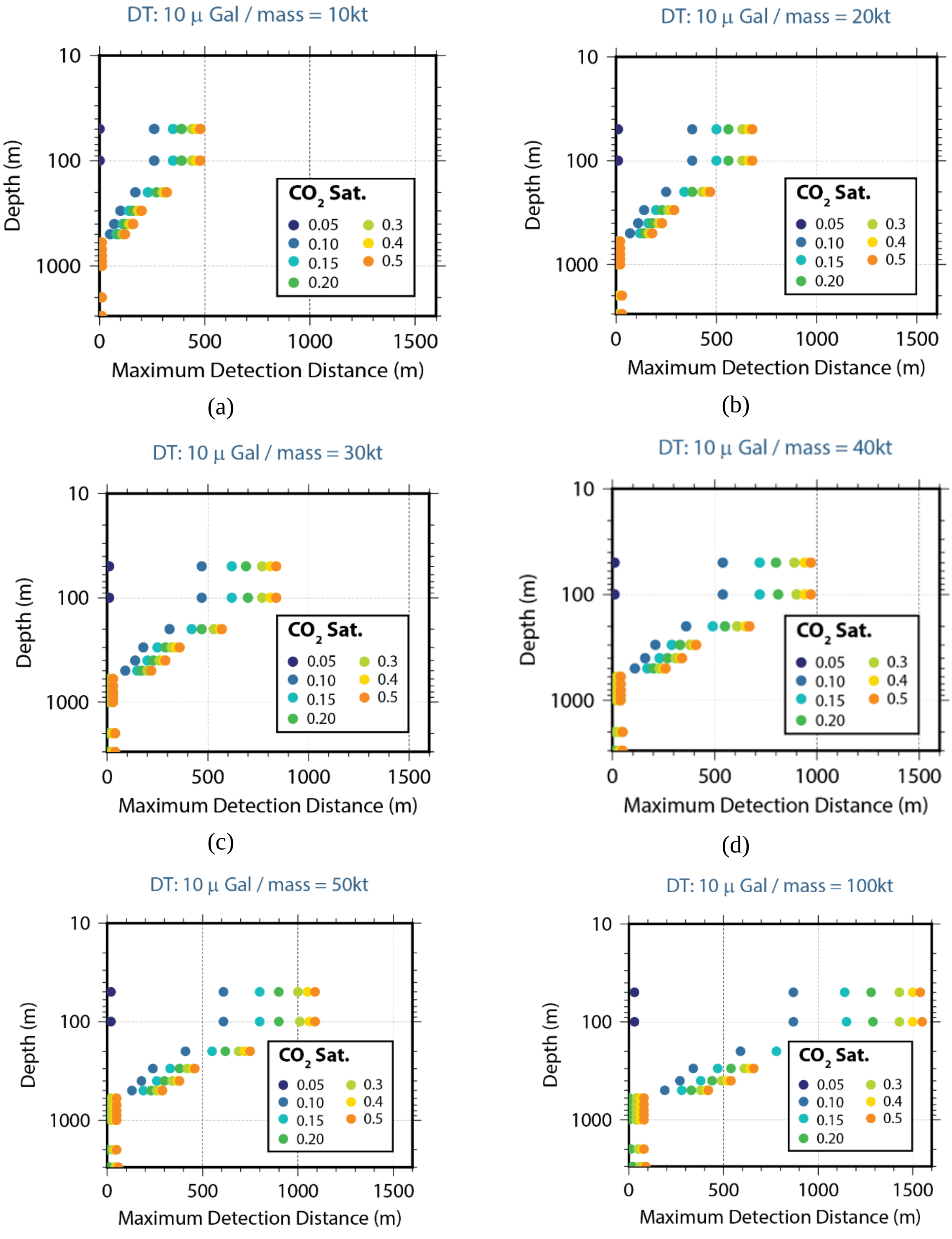

(a) (b)

(c) (d)

(e) (f)

Figure 33: Maximum distance of detection vs. depth of a 10-μGal change in the vertical gravity component g_z for (a) 10 kt, (b) 20 kt, (c) 30 kt, (d) 40 kt, (e) 50 kt, and (f) 100 kt CO_2 mass and CO_2 saturations varying from 0.05 to 0.5 (5–50%) (colored dots).

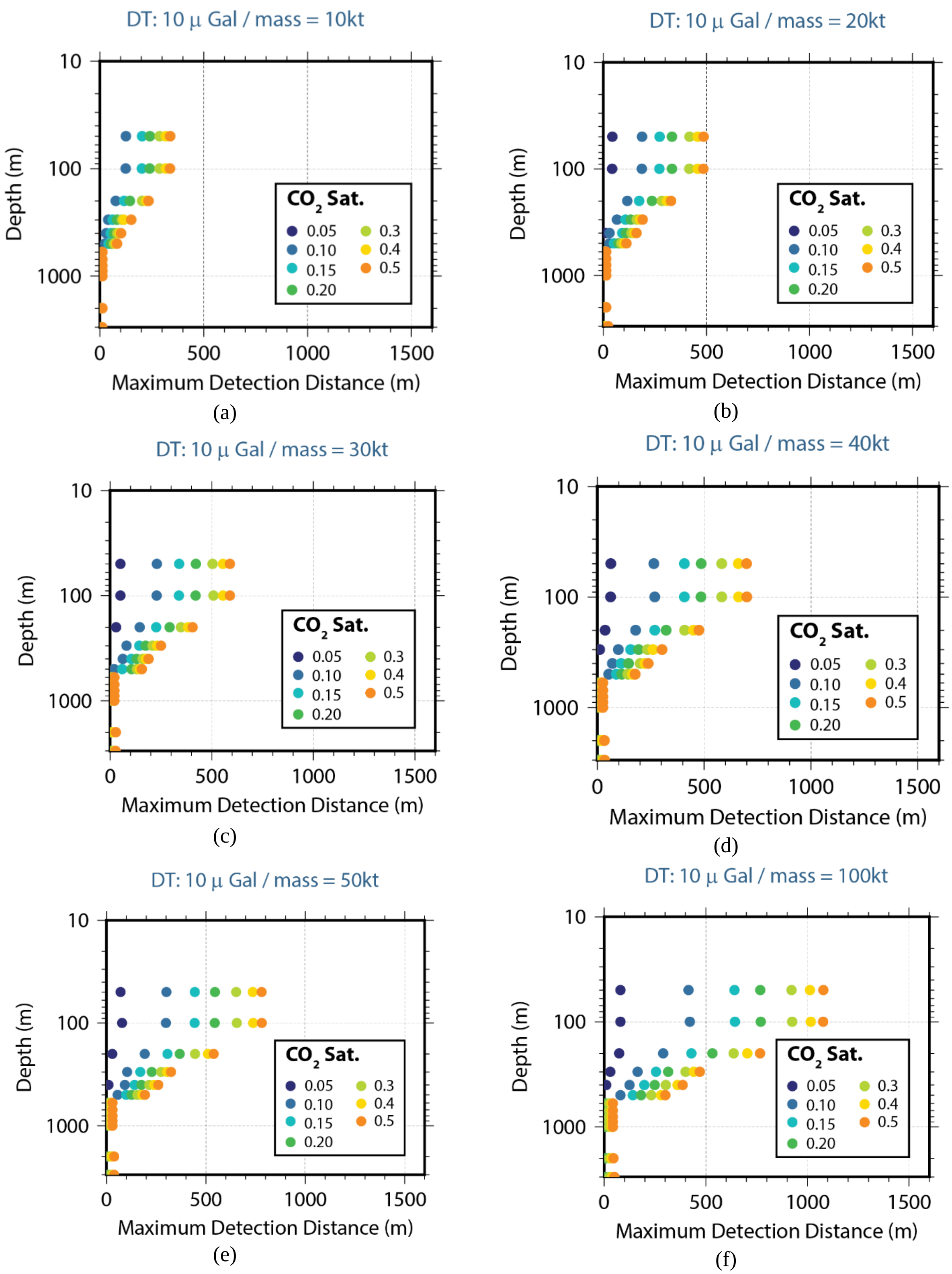

(a) (b) (c) (d) (e) (f)

Figure 34: Maximum distance of detection vs. depth of a 10-μGal change in the horizontal gravity component g_x for (a) 10 kt, (b) 20 kt, (c) 30 kt, (d) 40 kt, (e) 50 kt, and (f) 100 kt CO_2 mass and CO_2 saturations varying from 0.05 to 0.5 (5–50%) (colored dots).

5. ELECTRICAL AND ELECTROMAGNETIC MONITORING

5.1 BACKGROUND

Electrical and EM techniques measure electric (E) and magnetic (B or H) fields caused by currents that are injected into the ground by contacting electrodes or a time-varying magnetic field induced to flow into the ground by inductive sources. Electrical techniques, also called resistivity techniques, use only current and voltage measurements at frequencies low enough at which EM induction effects are negligible. EM techniques require frequency-dependent sources to induce currents in the ground. Magnetic fields are produced from currents created from both types of sources. When the earth's natural electromagnetic fields are used as a source the technique is called magnetotellurics (MT).

The goal of the monitoring survey is to identify changes in resistivity caused by a CO_2 plume displacing formation brine. The resistivity of CO_2 is high, similar to gas or air, while the resistivity of brine in deep brine-bearing formations is low. The relationship between fluid resistivity (ρ_w) and total dissolved solids (TDS) and temperature is shown in Figure 35. These anomalies would be formed if CO_2 moves into and replaces the brine in the formation.

The bulk electrical resistivity of the subsurface is highly sensitive to changes in key formation properties such as porosity, pore fluid resistivity, and fluid saturation. A wide range of empirical relations exists for linking formation and electrical properties. Archie's Law (Archie, 1942), which describes the electrical resistivity (ρ_b) of sedimentary rocks as a function of water saturation (S_w), porosity (ϕ), and pore fluid resistivity (ρ_w) is commonly used,

$$\rho_b = a\,\phi^{-m}\,\frac{\rho_w}{S_w^n}$$

where a is tortuosity, and m and n are constants with $1.8 < m < 2$ and $n \cong 2$.

Figure 36 shows the rock bulk resistivity (ρ_b) as a function of CO_2 saturation (S_{CO2}) for the formation with brine resistivity of 0.3 Ohm-m and 35% porosity. The replacement of highly conductive (low resistivity) saline fluids with resistive CO_2 results in resistivity increase in the formation. When CO_2 is present at shallow depths, dissolution of CO_2 causes an increase in TDS and results in resistivity decrease.

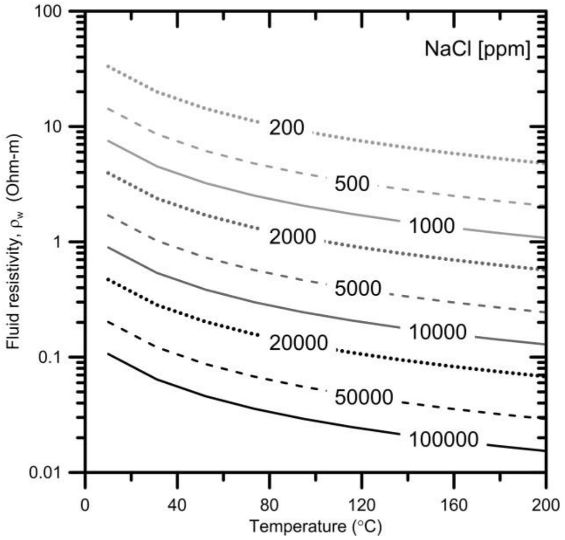

Figure 35: Fluid resistivity as a function of NaCl concentration and temperature.

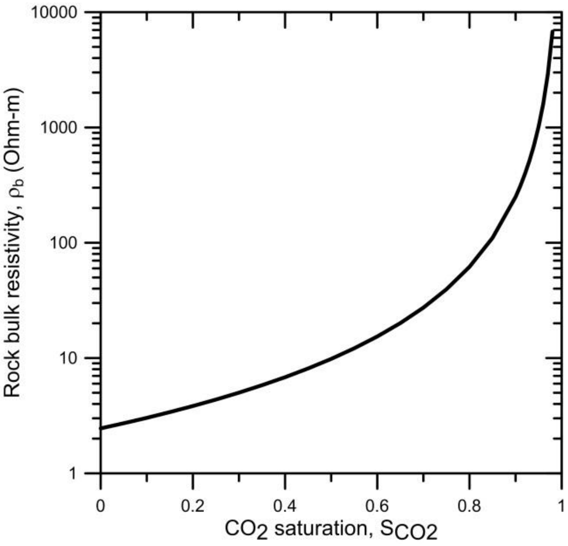

Figure 36: Rock bulk resistivity (ρ_b) as a function of CO_2 saturation (S_{CO2}). Pore fluid resistivity is 0.3 Ohm-m, porosity is 35%, a =1, m = 2, and n=2.

When CO_2 is injected into a formation originally filled with brine, electrical resistivity can be used to determine CO_2 saturation using the following:

$$S_{CO_2} = 1 - S_w = 1 - \frac{a\,\rho_w}{\varphi^m \rho_b}$$

or by the ratio of pre-injection (ρ_0) to monitored (ρ_b) resistivity (Carrigan et al., 2013):

$$S_{CO2} = 1 - \left(\frac{\rho_0}{\rho_b}\right)^{1/n},$$

where n is the saturation exponent, and 2.0 is the widely used default value.

When a formation contains a substantial amount of clay, an additional parameter—the ratio of volume of sand to volume of clay—is necessary (e.g., Nakatsuka et al., 2010).

Figure 37 illustrates a decrease in the response with increasing distance between the target and where the measurements are made using resistivity techniques.

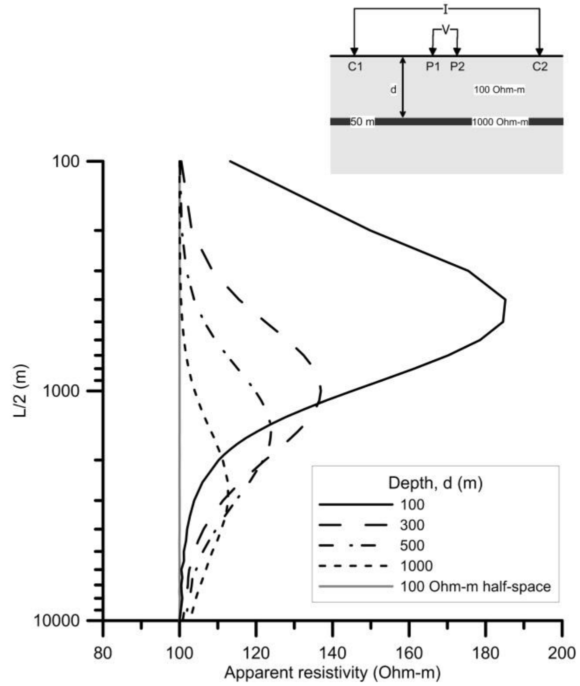

Figure 37: Apparent resistivity response of 1,000 Ohm-m and 50-m thick layer in a 100 Ohm-m half-space as a function of layer depth.

5.2 EM MONITORING FOR RESISTIVE TARGETS

Numerically simulated CO_2 plumes at the Kimberlina site in the San Joaquin Valley, California, were used to evaluate feasibility of using EM for time-lapse monitoring. As described in Section 2.2, these models include a primary CO_2 plume in the storage reservoir (depths of 2,800–1,600 m), and secondary plumes in three shallower formations (at depths from 200 to 1,600 m) developed by CO_2 migration through a dipping fault. Scenarios with the secondary plumes under supercritical CO_2 conditions in the lower two zones and under gas CO_2 conditions in the uppermost zone were studied. Both surface configurations and borehole-to-surface arrays were considered (Figure 38) with a focus on deep secondary CO_2 plumes tracking (Figure 39).

Controlled source EM (CSEM) surface configurations are more sensitive to shallow features, and thus in these scenarios detect the shallowest secondary CO_2 plumes only (red curve in Figure 38b). Borehole-to-surface CSEM configurations are more sensitive, and hence feasible for time-lapse monitoring and detection of CO_2 plumes at various depths (Figure 38c). These fit-for-purpose configurations would be suitable for early leak detection. The measured signal has to be above the detection threshold for tracking the plume with time (Figure 39c). Figure 39c illustrates that the monitoring signal at time-1 (yellow curve) is within the noise level, and hence would not be effective in detecting small amounts of CO_2 in the top and bottom layers of the formation (yellow outline in Figure 39a). Once the CO_2 fills the formation (magenta outline in Figure 39a) and forms a plume, the signal level is clearly (magenta curve) above the detection threshold and indicative of CO_2 plume presence. Depth and size of the secondary CO_2 plume plays an important role in the design. This illustrates that the monitoring well location is an important part of monitoring array design, as it should be to allow for monitoring of a region of interest.

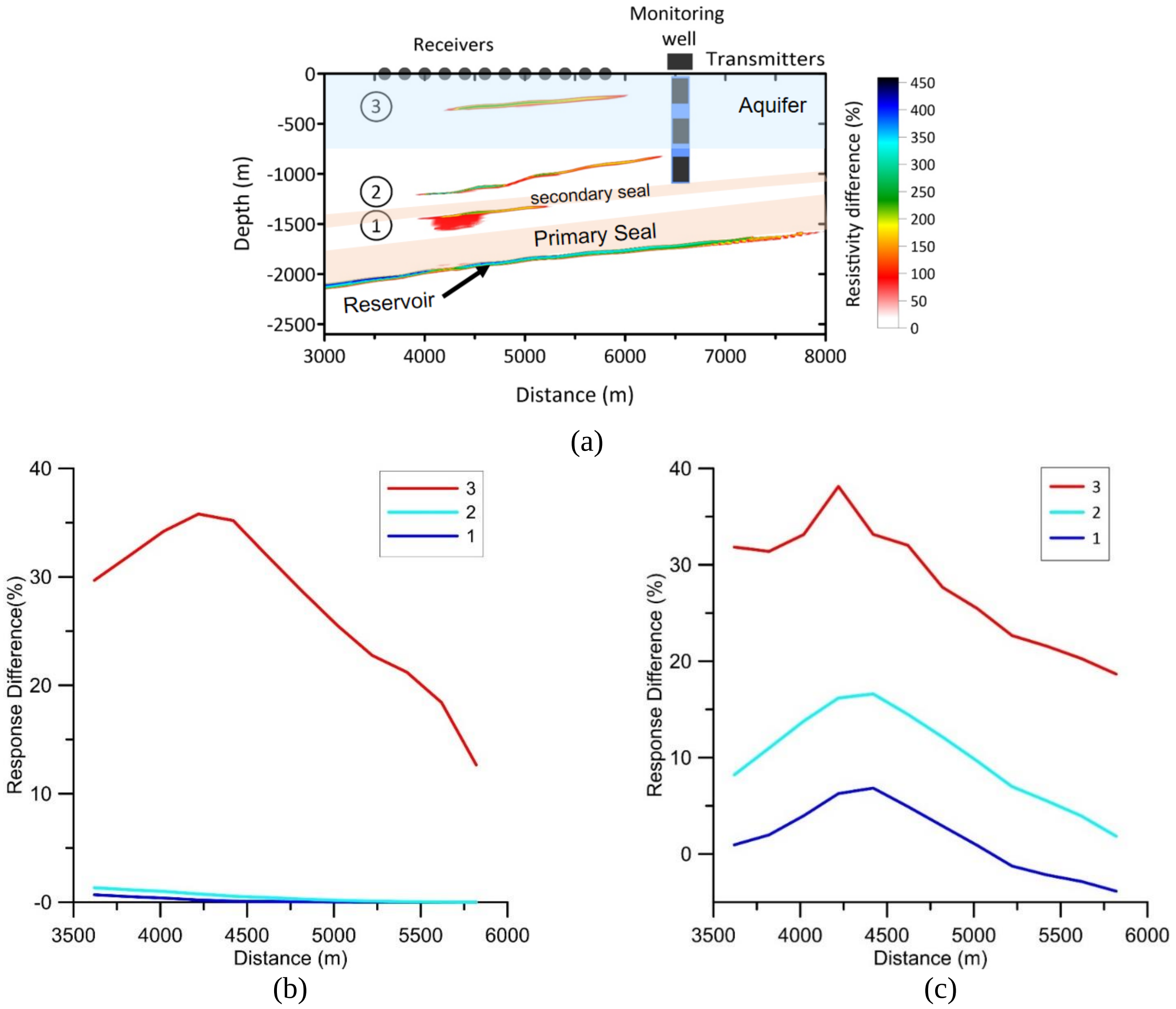

(a)

(b)

(c)

Figure 38: (a) Model with CO_2 plumes at different depths, (b) surface responses, and (c) borehole-to-surface responses due to CO_2 plumes in (a).

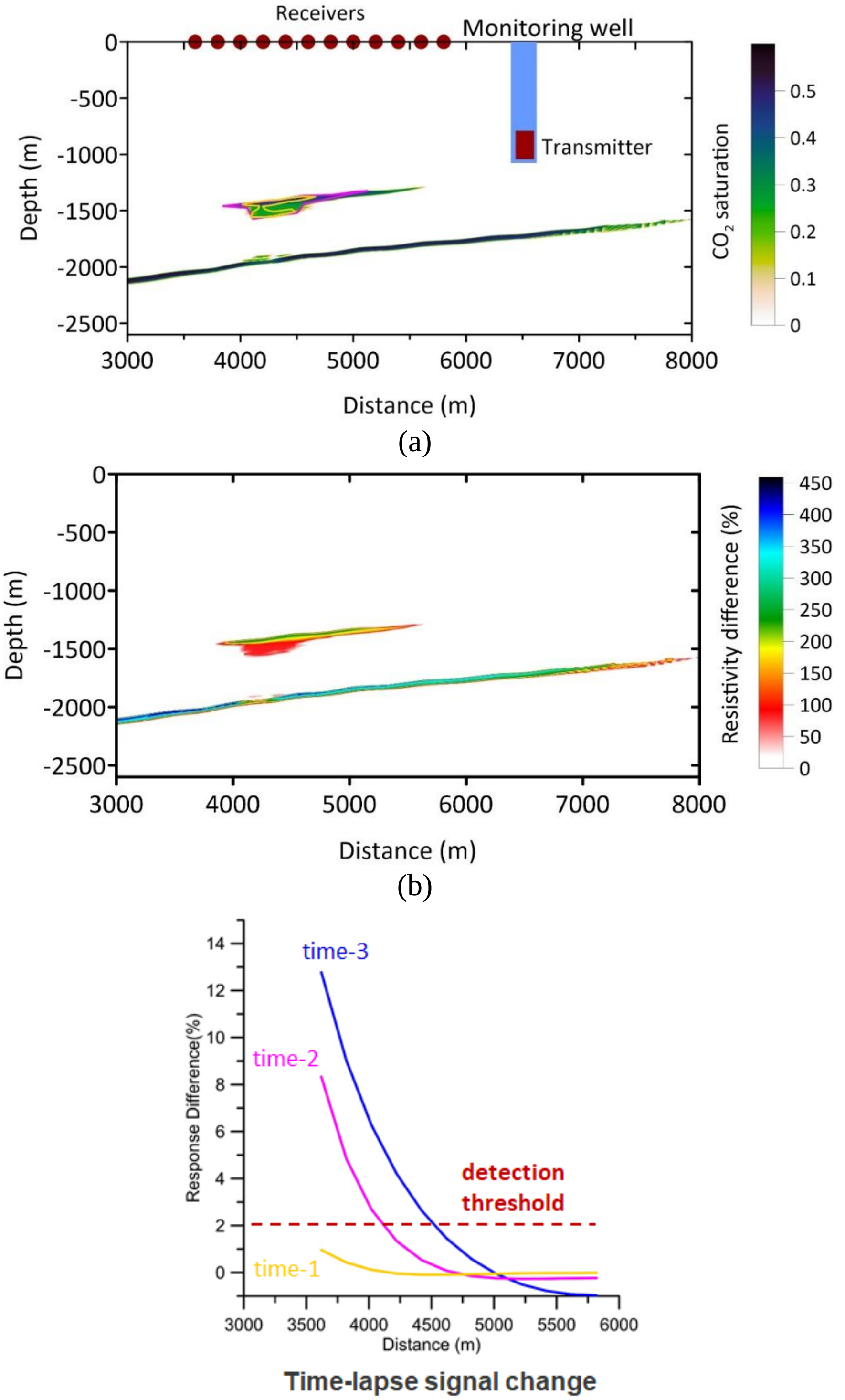

(a)

(b)

(c)

Figure 39: (a) Deep CO_2 plume model, (b) changes in subsurface resistivity due to CO_2 presence at time-3, and (c) changes in measured responses at three different times using borehole-to-surface configuration.

Figure 40 illustrates what might be possible if the goal is to estimate subsurface properties through an inversion of EM data. This figure shows 2D inversion result for another synthetic model (brown outline) similar to previous models. This result illustrates that while the location of the plume is recovered correctly (high resistivity values; warm colors), the subsurface resistivity distribution is overestimated at the top of the structure and underestimated at the deeper part of the structure.

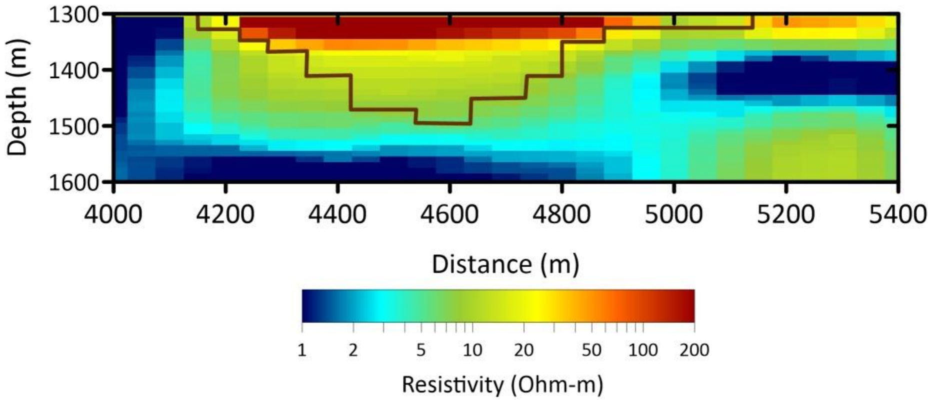

Figure 40: 2D EM inversion of synthetic data. True model is shown by brown outline.

An example of a successful field data acquisition is again from Sleipner. Marine CSEM data were acquired along a single line above the area of the CO_2 plume (Park et al., 2017). The total length of the towline was ~30 km, with EM source towed just above the seabed, ~10 km beyond the receiver array. The receivers were deployed on the seabed with 500 m spacing. The quality of the EM data was excellent, and processing enabled the removal of unwanted signal from the seabed pipelines. The lateral extension of the CO_2 plume was well captured by the EM data inversion. There was also good agreement between the seismic image and the EM inversion results, albeit without resolving detailed layering and the exact depth of the CO_2 plume because of much lower EM resolution. These results suggest that the marine CSEM can be an important tool for offshore CO_2 storage monitoring, especially when combined with seismic and gravity.

These fit-for-purpose borehole-to-surface CSEM monitoring arrays are suitable for monitoring over large areas, but have yet to be tested at actual sites. Some traditional and established techniques, e.g., electrical resistance tomography (ERT), were used at early CO_2 injection pilot sites. An example of a successful ERT deployment was an experimental cross-well ERT system operated successfully for more than 1 year obtaining time lapse electrical resistivity images during the injection of approximately 1-million tons of CO_2 at a depth exceeding 3,000 m in an oil and gas field in Cranfield, Mississippi (Carrigan et al., 2013). Furthermore, it is important to point out that these ERT results were the first to suggest that the site conceptual model was more complicated than first assumed (Zhou et al., 2019). The first long-term evaluation of a technical performance of the ERT electrode array was done at the Ketzin site (e.g., Schmidt-Hattenberger et al., 2016 and references therein) for monitoring of a reservoir at the depth of 600 m. The permanent ERT array operated for more than 7 years, including 5 years of the CO_2 injection. Both experiments and many others demonstrated the value of cross-well ERT in subsurface imaging on a small scale because of measurements proximity to the target of interest. The aspect ratio (borehole spacing/instrumented wellbore length) should be <0.75 in order to get tomographic results with sufficient image resolution (LaBrecque et al.,1996). The disadvantage of cross-well ERT arrays is their limited areal coverage, which makes them unsuitable for monitoring over large areas.

5.3 EM MONITORING FOR CONDUCTIVE TARGETS

Synthetic model scenarios were based on a hypothetical, commercial-scale GCS reservoir at the Kimberlina site in the southern San Joaquin Basin, California, where CO_2 and brine leak through legacy well into shallow aquifers, as described in Section 2.2. Over 900 aquifer impact datasets were used to capture the uncertainty in the subsurface geology and leakage scenarios. Brine and CO_2 leakage results in subsurface changes in pressure, CO_2 saturation, and TDS. CO_2 buoyancy allows a significant fraction of CO_2 to reach shallower permeable zones. An example of one such scenario is shown in Figure 41.

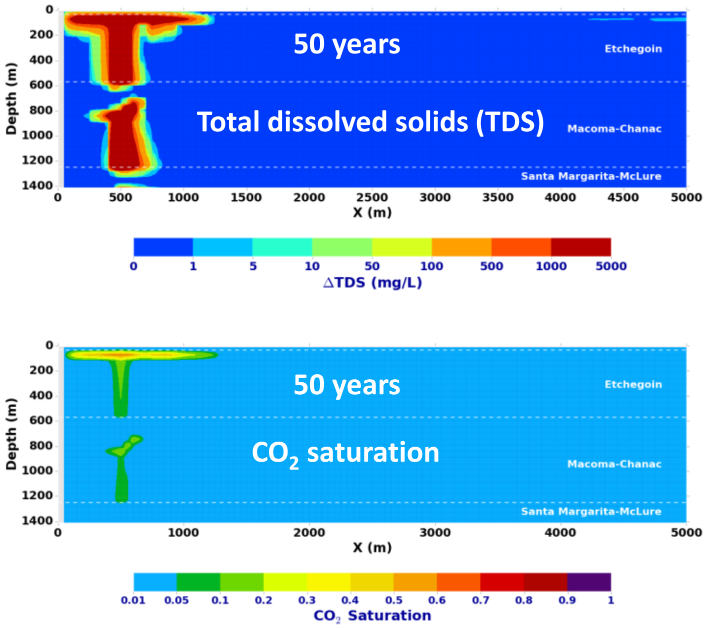

Figure 41: Contour plots of TDS increase above background (top) and CO_2 saturation (bottom) are shown at 50 years for a leaking well 1 km from the CO_2 injector, a high groundwater gradient, high wellbore permeability, and two leaky aquifers.

Forward simulations were done using 2D ERT profile with 40-m electrodes spacing run along the center line of leakage plumes, which intersects the leaky wellbore. The profile was 3,000-m long, which gives an approximate depth of penetration at 600 m (Yang et al., 2019). MT data were simulated along the same profile with 250-m station spacing.

In a shallow aquifer, dissolved CO_2 lowers fluid resistivity, but gas-phase CO_2 increases formation resistivity. These two opposite effects cancel each other to a certain extent, but dissolved CO_2 has a greater impact on formation resistivity, which results in overall decrease of formation resistivity (Yang et al., 2015).

The results are shown in Figure 42. Detection thresholds of 10% and 20% change in apparent resitivity for ERT and MT, respectively, were used in this study. The smallest detectable mass is indicated by the vertical dotted red line in Figures 42a and 42b, indicating that both techniques can detect a CO_2 leakage of 20 kt or larger.

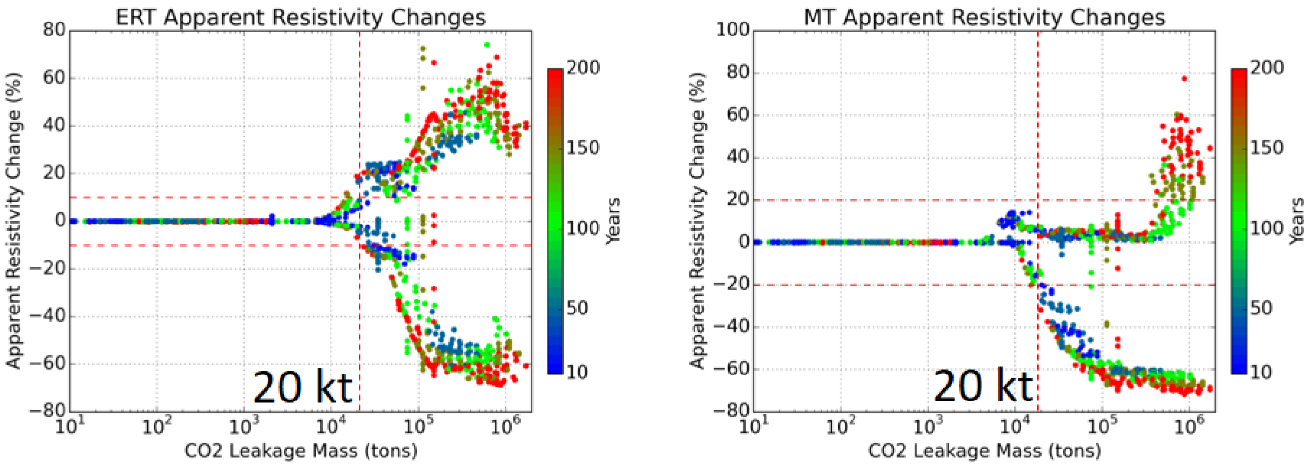

(a) (b)

Figure 42: Apparent resistivity change as a function of CO_2 leakage mass for (a) ERT and (b) MT. Colors represent time steps.

Figure 43 shows the changes in apparent resisitivity as a function of CO_2 saturation for ERT (Figure 43a) and MT (Figure 43b) techniques. The colors and symbols indicate the plume depth and volume. Both techniques are sensitive to the same subsurface properties, and the results are comparable. In general, only shallow and large plumes with a high CO_2 saturaton are above a detection threshold. With the configurations used in these studies, the plumes below 600 m are not detectable. The volume reported here is the impacted rock volume, which is different (and much larger) from CO_2 volumes reported in other scenarios. The choice of which technique to use for site monitoring would depend on site conditions and the budget. As mentioned in the introduction, ERT might be more sensitive to shallow subsurface, but the deployment and acquisition are more labor intensive. The use of MT would be driven by the depth of the interest, as the measured signal depends on natural signal strength. If the main target/zone of interest is at depths (e.g., 1,500–2,000 m) that are resolved by signals at frequencies within a low-natural-signal band, and that signal is low, MT might not be sensitive to small subsurface changes due to high levels of data noise.

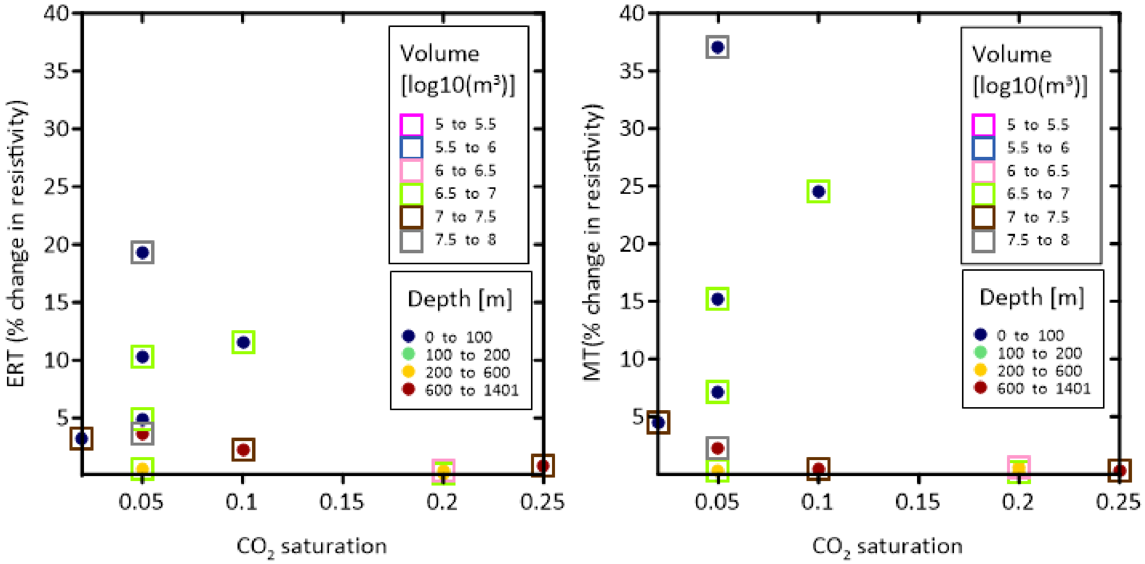

Figure 43: Change is resistivity as a function of CO_2 saturation for (a) ERT and (b) MT.

6. SUMMARY

The use of 4D seismic to monitor injected CO_2 was best demonstrated by the Sleipner project, which has been conducting 3D seismic surveys over an increasing volume of injected CO_2 since the mid-1990s. This study focused on early detection of secondary CO_2 plumes, which meant imaging much smaller volumes of CO_2 than in the case of Sleipner. The size of the secondary CO_2 plume that is detectable strongly depends on the survey geometry, field conditions, and data processing. A trade-off between the sensitivity to an expected plume size and cost may play an important role in designing monitoring arrays at GCS sites.

VSP is an established tool for imaging and monitoring in the vicinity of accessible boreholes (those which can be entered for sensor deployment). Typically, VSP offers improved spatial resolution and lower cost, as compared to surface seismic. The applicability of VSP to CO_2 storage monitoring has been well established by many projects. The use of permanent fiber deployment in a well offers very low-cost, highly repeatable VSPs using DAS. For long-term monitoring, the advantages of permanent DAS are considerable. DAS technology is developing with the gap between convectional sensors and DAS closing rapidly.

In general, VSP data, like surface seismic data, are typically interpreted qualitatively using some measure of change in seismic property to delineate a CO_2 plume and estimate the spatial variability in CO_2 saturation without quantitative estimates. Qualitative detection of CO_2 from VSPs has been successful following injection of less than 1 kt to 5 kt, with more common detection after 10 s of kt. Plumes of 10- to 100-m diameter have been delineated. Quantitative estimation of the spatial variation in CO_2 saturation has been performed; however, uncertainty in rock properties, rock physics models, and geochemical alteration, as wells as unknown heterogeneity, add to uncertainty in the quantitative results. For the Otway project, analysis of surface seismic indicates that plumes of 10–30 kt, with diameters of 100–200 m, can be detected with moderate data quality, and it is reasonable to expect VSP to have similar results within the vicinity of a monitoring well.

While most small-scale CO_2 projects have used a single monitoring well for VSP, typically near the injection well, it is likely that large scale projects would use multiple wells. The use of fiber optic sensing opens the possibility of low-cost small diameter (1–2 in.) boreholes with fiber cables strategically placed to monitor the expanding perimeter or local areas of concern. In this way, VSP can provide a method of monitoring CO_2 plumes as they grow or migrate.

Earlier numerical studies demonstrated that time-lapse gravity could be successfully applied as a monitoring tool for GCS. The first deployment of time-lapse gravity surveys at an actual storage site on the sea floor was implemented at the Sleipner site. The repeated surveys allowed gravity anomalies larger than 10 μGal to be detected, and constrained the density of the injected CO_2 and the rate of dissolution. However, the depth of CO_2 injection operations, generally deeper than 800 m, and the error associated with gravity surveys (typically 5 μGal), limit the performance of surface measurements. To obtain stronger gravity responses, borehole gravity surveys have been suggested as a method to overcome this challenge. Borehole gravity surveys applied to GCS have been numerically assessed, but only a limited number of field tests have been undertaken. The most documented study was done for the field test conducted at the Cranfield site, Mississippi. That field test yielded results about density changes associated with CO_2 injection in a complex geologic environment.

Recent engineering advances in gravimeter technology, for use both at the ground surface and in boreholes, could significantly change the landscape regarding the use of time-lapse gravity measurements as an efficient and cost-effective method for monitoring subsurface processes. Detection of gravity variations accompanying mass redistributions in the subsurface caused by fluid movements in reservoirs provides a unique means for monitoring the dynamics of a carbon sequestration site. More specifically, it has been recognized as a way to estimate the total amount of stored CO_2 that can complement the areal definition provided by seismic methods to determine the volume or saturation of CO_2 plumes.

Time-lapse gravity monitoring at the surface or in boreholes can provide fundamental information related to general behavior of the GCS site, thus providing data used in demonstrating conformance. The gravity method is the only geophysical method that can provide a direct estimate of CO_2 mass distribution at depth. A decision whether gravity would be included in a monitoring portfolio will be site specific, and depend on an expected size and depth of the CO_2 plume of interest. The gravity response is inversely proportional to the squared distance, hence the closer the sensors are to the CO_2 plume, the smaller the plume size that can be detected. When considering long-term monitoring costs, gravity monitoring has the advantage of being relatively inexpensive compared to other methods.

Electrical and EM techniques infer the distribution of electrical resistivity in the subsurface from measured electric and magnetic fields. The electrical resistivity of the subsurface is highly sensitive to changes in formation properties such as porosity, pore fluid resistivity, and fluid saturation. Resistivity techniques are much more sensitive to low resistivities (conductive targets), and hence deep resistive targets are much more difficult to detect. The response to a shallow conductive target is an order of magnitude larger than to the deep resistive target. There are many possible configurations of sources (transmitters) and receivers (sensors). Depth and size of the secondary CO_2 plume will play an important role in the site specific, fit-for-purpose, monitoring array design. The advantage of passive techniques (e.g., MT) is an ease of deployment in the field, and that there are no source/configuration artifacts present in the data. However, as the natural field strength varies, these fields might not be large enough to produce measurable secondary signals from the regions of interest. The configurations using the active source can be optimized for required spatial resolution, but the field deployment is more expensive and advanced data processing is required.

7. REFERENCES

Ahamadi, A. B. Analysis of Time-Lapse 3-D VSP Data for Seismic Monitoring of CO_2 Flood in Weyburn Field, Saskatchewan. PhD Thesis, University of Saskatchewan, 2016.

Alnes, H.; Eiken, O.; Nooner, S.; Sasagawa, G.; Stenvold, T.; Zumberge, M. Results from Sleipner gravity monitoring: Updated density and temperature distribution of the CO_2 plume. *Energy Procedia* **2011,** *4*, 5504–5511.

Alnes, H.; Eiken, O.; Stenvold, T. Monitoring gas production and CO_2 injection at the Sleipner field using time-lapse gravimetry. *Geophysics* **2008,** *73*, WA155–WA161.

Appriou, D.; Bonneville, A.; Zhou, Q.; Gasperikova, E. Assessment of time-lapse gravity monitoring for detecting CO_2 leakage from a faulted subsurface storage complex. *International Journal of Greenhouse Gas Control* **2020,** *95*, 102956. https://doi.org/10.1016/j.ijggc.2020.102956

Archie, G. E. The electrical resistivity log as an aid in determining some reservoir characteristics. *T Am I Min Met Eng* **1942,** *146*, 54–61.

Balch, A. H. *Vertical Seismic Profiling: Technique Applications and Case Histories*, 1984th ed.; Balch, A. H., Lee, M. W., Eds.; International Human Resources Development Corporation, 1984.

Barnola, A. S.; Ibram, M. 3D simultaneous joint PP-PS prestack seismic inversion at Schiehallion field, United Kingdom Continental Shelf. *Geophysical Prospecting* **2014,** *62*, 278–292.

Bauer, R. A.; Will, R.; Greenberg, S. E.; Whittaker, S. G. *Illinois Basin – Decatur Project, In: Geophysics and Geosequestration*, Davis, T. L., Landro, M., Wilson, M., Eds.; Cambridge University Press, 2019.

Butler, E.; Mueller, S.; Davis, T. L. Application of time-lapse multi-component seismic inversion to characterize pressure and stimulation in the Niobrara and Codell reservoirs, Wattenberg Field, Colorado. *First Break* **2016,** *34*.

Carrigan, C. R; Yang, X.; LaBrecque, D. J.; Larsen, D.; Freeman, D.; Ramirez, A. L.; Daily, W.; Aines, R.; Newmark, R.; Friedmann, J.; Hovorka, S. Electrical resistance tomographic monitoring of CO_2 movement in deep geologic reservoirs. *International Journal of Greenhouse Gas Control* **2013,** *18*, 401–408.

Chadwick, A.; Williams, G.; Delepine, N.; Clochard, V.; Labat, K.; Sturton, S.; Buddensiek, M.-L.; Dillen, M.; Nickel, M.; Lima, A. L.; Arts, R.; Neele, F.; Rossi, G. Quantitative Analysis of Time-Lapse Seismic Monitoring Data at the Sleipner CO_2 Storage Operation. *Lead. Edge* **2010,** *29*, 170–177.

Chadwick, R. A.; Noy, D. J. Underground CO_2 storage: demonstrating regulatory conformance by convergence of history-matched modeled and observed CO_2 plume behavior using Sleipner time-lapse seismics. *Greenhouse Gas Sci Technol* **2015,** *5*, 305–322.

Clochard, V.; DeVault, B. C.; Bowen, D.; Delépine, N.; Wangkawong, K. Quadri-joint inversion: Method and application to the Big Sky 9C 3D data set in northern Montana. *Interpretation* **2018,** *6*, SN101–SN118.

Coueslan, M. L.; Ali, S.; Campbell, A. Monitoring CO_2 injection for carbon capture and storage using time-lapse VSPs. *The Leading Edge* **2013,** *32*, 1268-1276.

Daley, T. M. Rock Physics of CO_2 storage monitoring in Porous media. In *Geophysics and Geosequestration*; Davis, T. L.; Landro, M.; Wilson, M., Eds.; Cambridge University Press, 2019.

Daley, T. M.; Hendrickson, J.; Queen, J. H. Monitoring CO_2 Storage at Cranfield, Mississippi with Time-Lapse Offset VSP – Using Integration and Modeling to Reduce Uncertainty. *Energy Procedia* **2014,** *63*, 4240–4248.

Daley, T. M.; Miller, D. E.; Dodds, K.; Cook, P.; Freifeld, B. M. Field Testing of Modular Borehole Monitoring with Simultaneous Distributed Acoustic Sensing and Geophone Vertical Seismic Profile at Citronelle, Alabama. *Geophysical Prospecting* **2016,** *64*, 1318–1334.

Daley, T. M.; Myer, L. R.; Peterson, J. E.; Majer, E. L.; Hoversten, G. M. Time-lapse crosswell seismic and VSP monitoring of injected CO_2 in a brine aquifer. *Environmental Geology* **2008,** *54*, 1657–1665.

Dariu, H.; Garotta, R.; Granger, P. Y. Simultaneous inversion of PP and PS wave AVO/AVA data using simulated annealing. 73rd SEG Annual International Meeting. *Expanded Abstracts* **2003,** *22*, 120–123.

Davis, T., Landrø, M., Wilson M., Eds.; *Geophysics and Geosequestration*. Cambridge: Cambridge University Press, 2019.

Diao, Y.; Zhu, G.; Li, X.; Bai, B. Characterizing CO_2 plume migration in multi-layer reservoirs with strong heterogeneity and low permeability using time-lapse 2D VSP technology and numerical simulation. *International Journal of Greenhouse Gas Control* **2020,** *92*, 102880.

Dodds, K.; Krahenbuhl, R.; Reitz, A.; Li, Y.; Hovorka, S. Evaluating time-lapse borehole gravity for CO_2 plume detection at SECARB Cranfield. *International Journal of Greenhouse Gas Control* **2013,** *18*, 421–429.

Dubey, C. P.; Tiwari, V. M. Computation of the gravity field and its gradient: Some applications. *Computers & Geosciences* **2016,** *88*, 83–96.

Eiken, O.; Stenvold, T.; Zumberge, M.; Alnes, H.; Sasagawa, G. Gravimetric monitoring of gas production from the Troll field. *Geophysics* **2008,** *73*, WA149–WA154.

Ferguson, J. F.; Klopping, F. J.; Chen, T.; Seibert, J. E.; Hare, J. L.; Brady J. L. The 4D microgravity method for waterflood surveillance: Part 3 - 4D absolute microgravity surveys at Prudhoe Bay, Alaska. *Geophysics* **2008,** *73*, WA163–WA171.

Furre, A. K.; Eiken, O.; Alnes, H.; Vevatne, J. N.; Kiær, A. F. 20 Years of Monitoring CO_2-injection at Sleipner. *Energy Procedia* **2017,** *114*, 3916–3926.

Galperin, E. I. Vertical Seismic Profiling and Its Exploration Potential. In *Seismology and Exploration Geophysics*. Springer, Dordrecht, 1985; Vol 1.

Garotta, R.; Granger, P. Y.; Dariu, H. Combined interpretation of PP and PS data provides direct access to elastic rock properties. *The Leading Edge* **2002,** *21*, 532–535.

Gasperikova, E.; Hoversten, G. M. Gravity monitoring of CO_2 movement during sequestration: model studies. *Geophysics* **2008,** *73*, WA105–WA112.

Glubokovskikh, S.; Pevzner, R.; Gunning, J.; Dance, T.; Shulakova, V.; Popik, D.; Popik, S.; Bagheri, M.; Gurevich, B. How well can time-lapse seismic characterize a small CO_2 leakage into a saline aquifer: CO2CRC Otway 2C experiment (Victoria, Australia). *International Journal of Greenhouse Gas Control* **2020,** *92*, 102854.

Gotz, J.; Luth, S.; Krawczyk, C.; Cosma, C. Zero-Offset VSP Monitoring of CO_2 Storage: Impedance Inversion and Wedge Modelling at the Ketzin Pilot Site. *International Journal of Geophysics* **2014,** Article ID 294717. http://dx.doi.org/10.1155/2014/294717

Hardage, B. A. *Vertical seismic profiling, Part A: Principles*; Geophysical Press, 1983.

Hardage, B. A.; DeAngelo, M. V.; Murray, P. E; Sava, D. *Multicomponent seismic technology;* Society of Exploration Geophysicists, 2011.

Hare, J. L.; Ferguson, J. F.; Aiken, C. L. V.; Brady, J. L. The 4-D microgravity method for waterflood surveillance: A model study for the Prudhoe Bay reservoir, Alaska. *Geophysics* **1999,** *64*, 78–87.

Harris, K.; White, D.; Samson, C. 4D VSP monitoring at the Aquistore CO_2 storage site, *Geophysics* **2017,** *82*, M81–M96.

Hoversten, G. M.; Commer, M.; Haber, E.; Schwarzbach, C. Hydro-frac monitoring using ground time-domain electromagnetics. *Geophysical Prospecting* **2015,** *63*, 1508–1526.

Hovorka, S. D.; Meckel, T. A.; Trevino, R. H.; Lu, J.; Nicot, J.-P.; Choi, J.-W.; Freeman, D.; Cook, P.; Daley, T. M.; Ajo-Franklin, J. B.; Freifeild, B. M.; Doughty, C.; Carrigan, C.R.; La Brecque, D.; Kharaka, Y. K; Thordsen, J. J.; Phelps, T. J.; Yang, C.; Romanak, K. D.; Zhang, T.; Holt, R. M.; Lindler, J. S.; Butsch, R. J. Monitoring a large volume CO2 injection: Year two results from SECARB project at Denbury's Cranfield, Mississippi, USA, *Energy Procedia* **2011,** *4*, 3478–3485.

Ivanova, A.; Kashubin, A.; Juhojuntti, N.; Kummerow, J.; Henninges, J.; Juhlin, C.; Lüth, S.; Ivandic, M. Monitoring and volumetric estimation of injected CO_2 using 4D seismic, petrophysical data, core measurements and well logging: a case study at Ketzin, Germany. *Geophysical Prospecting* **2012,** *60*, 957–973.

Jacob, T.; Bayer, R.; Chery, J.; Le Moigne, N. Time-lapse microgravity surveys reveal water storage heterogeneity of a karst aquifer. *Journal of Geophysical Research: Solid Earth* **2010,** *115*, B06402.

Jacob, T.; Rohmer, J.; Manceau, J. C. Using surface and borehole time-lapse gravity to monitor CO_2 in saline aquifers: a numerical feasibility study. *Greenhouse Gases: Science and Technology* **2016,** *6*, 34–54.

Kragh, E.; Christie, P. Seismic repeatability, normalised RMS, and predictability. *The Leading Edge* **2002,** *21*, 640–647.

Krahenbuhl, R. A.; Li, Y. Time-lapse gravity: A numerical demonstration using robust inversion and joint interpretation of 4D surface and borehole data. Geophysics **2012**, *77*, G33–G43.

Krahenbuhl, R. A.; Martinez, C.; Li, Y.; Flanagan, G. Time-lapse monitoring of CO_2 sequestration: A site investigation through integration of reservoir properties, seismic imaging, and borehole and surface gravity data. *Geophysics* **2015,** *80*, WA15–WA24.

LaBrecque, D. J.; Ramirez, A. I.; Daily, W. D.; Binley, A. M.; Schima, S. A. ERT monitoring of environmental remediation processes. *Meas. Sci. Technol.* **1996,** *7*, 375–383.

Landro, M. Repeatability issues of 3-D VSP data. *Geophysics* **1999,** *64*, 1673–1679.

Lebrun, D.; Richard, V.; Mace, D.; Cuer, M. SVD for multi-offset linearized inversion: Resolution analysis in multicomponent acquisition. *Geophysics* **2001,** *66*, 871–882.

Lemmon, E. W.; McLinden, M. O.; Friend, D. G. *Thermophysical Properties of Fluid Systems, edited*, Gaithersburg MD, 20899, USA, National Institute of Standards and Technology **2018**. doi:10.18434/T4D303.

Li, L.; Ma, J. F.; Wang, H. F.; Tan, M. Y.; Cui, S. L.; Zhang, Y. Y.; Qu, Z. P. Shear wave velocity prediction during CO_2-EOR and sequestration in the Gao89 well block of the Shengli Oilfield. *Applied Geophysics* **2017,** *14*, 372-380.

Nakatsuka, Y.; Xue, Z.; Garcia, H.; Matsuoka, T. Experimental study on CO_2 monitoring and quantification of stored CO_2 in saline formations using resistivity measurements. *International Journal of Greenhouse Gas Control* **2010,** *4*, 209–216.

Nazari, S.; Daley, T. M. *Assessing Uncertainty and Repeatability in Time-lapse VSP Monitoring of CO_2 Injection in a Brine Aquifer, Frio Formation, Texas (A case study);* Report LBNL-6482E; Lawrence Berkeley National Laboratory, Berkeley, CA, 2013.

NIST. NIST Mixture Property Database, NIST Standard Reference Database #14; U.S. Department of Commence, National Institute of Standards and Technology (NIST), 1992.

Nooner, S. L.; Eiken, O.; Hermanrud, C.; Sasagawa, G. S.; Stenvold, T.; Zumberge, M. A. Constraints on the in situ density of CO_2 within the Utsira formation from time-lapse seafloor gravity measurements. *International Journal of Greenhouse Gas Control* **2007,** *1*, 198–214.

Nur, A. M.; Wang, Z. In-Situ Seismic Monitoring EOR: The Petrophysical Basis. In *SPE Annual Technical Conference and Exhibition*; SPE-16865, Society of Petroleum Engineers, 1987.

Park, J.; Sauvin, G.; Vöge, M. 2.5D Inversion and Joint Interpretation of CSEM Data at Sleipner CO_2 Storage. *Energy Procedia* **2017,** *114*, 3989–3996.

Pevzner, R.; Caspari, E.; Gurevich, B.; Dance, T.; Cinar, Y. Feasibility of CO_2 plume detection using 4D seismic: CO2CRC Otway Project case study - Part 2: Detectability analysis. *Geophysics* **2015,** *80*, B105–B114.

Pevzner, R.; Urosevic, M.; Popik, D.; Tertyshnikov, K.; Caspari, E.; Correa, J.; Kepic, A.; Glubokovskikh, S.; Ziramov, S.; Gurevich, B.; Shulakova, V.; Dance, T.; Singh, R. Seismic monitoring of CO_2 geosequestration: preliminary results from Stage 2C of the CO2CRC Otway Project one year post injection. *SEG Technical Program Expanded Abstracts* **2017,** 5895–5900.

Popik, S.; Pevzner, R.; Tertyshnikov, K.; Popik, D.; Urosevic, M.; Shulakova, V.; Glubokovskikh, S.;Gurevich, B. 4D surface seismic monitoring the evolution of a small

CO_2 plume during and after injection: CO2CRC Otway Project study. *Exploration Geophysics* **2020**. doi: 10.1080/08123985.2020.1735934.

Popta, J. V.; Heywood, J. M. T.; Adams, S. J.; Bostock, D. R. Use of borehole gravimetry for reservoir characterization and fluid saturation monitoring. In *European Petroleum Conference*; Society of Petroleum Engineers paper 20896, 1990.

Schlumberger. https://www.glossary.oilfield.slb.com/en/Terms/v/vertical_seismic_profile.aspx (accessed on Nov 3, 2020).

Schmidt-Hattenberger, C.; Bergmann, P.; Labitzke, T.; Wagner, F.; Rippe, D. Permanent crosshole electrical resistivity tomography (ERT) as an established method for the long-term CO_2 monitoring at the Ketzin pilot site. *International Journal of Greenhouse Gas Control* **2016,** *52*, 432–448.

Singh, P.; Davis, T. Advantages of shear wave seismic in Morrow sandstone detection. *International Journal of Geophysics* **2011,** *16*.

Singh, P.; Davis, T. L.; DeVault, B. Poststack, prestack, and joint inversion of P-and S-wave data for Morrow A sandstone characterization. *Interpretation* **2015,** *3*, SZ59–SZ92.

Streich, R.; Becken, M.; Ritter, O. Imaging of CO_2 storage sites, geothermal reservoirs, and gas shales using controlled-source magnetotellurics: modeling studies. *Chem Erde-Geochem* **2010,** *70*, 63–75.

Van Dok, R.; Gaiser, J. Stratigraphic description of the Morrow Formation using mode-converted shear waves: Interpretation tools and techniques for three land surveys. *The Leading Edge* **2001,** *20*, 1042–1047.

Wang, Z.; Cates, M. E.; Langan, R. T. Seismic monitoring of a CO_2 flood in a carbonate reservoir: A rock physics study. *Geophysics* **1998,** *63*, 1604–1617.

Wang, Z.; Harbert, W.; Dilmore, R.; Huang, L. Modeling of time-lapse seismic monitoring using CO_2 leakage simulations for a model CO_2 storage site with realistic geology: Application in assessment of early leak-detection capabilities. *International Journal of Greenhouse Gas Control* **2018,** *76*, 39–52.

White, D. Integrated Geophysical Characterization and Monitoring at the Aquistore CO_2 Storage Site. In *Geophysics and Geosequestration*; Davis, T. L., Landro, M., Wilson, M., Eds.; Cambridge University Press, 2019.

White, D. Personal communication, 2020.

White, D.; Harris, K.; Roach, L.; Cheraghi, S.; Roberts, B.; Daley, T. M.; Robertson, M. Tracking a deep CO_2 plume: 4D seismic imaging at the Aquistore CO_2 storage site, Saskatchewan, Canada. *14th International Conference on Greenhouse Gas Control Technologies* **2018,** GHGT-14.

Yang, X.; Buscheck, T. A.; Mansoor, K.; Carroll, S. A. Assessment of Geophysical Monitoring Methods for Detection of Brine and CO_2 Leakage in Drinking Aquifers. *International Journal of Greenhouse Gas Control* **2019,** *90*, 102803. https://doi.org/10.1016/j.ijggc.2019.102803.

Yang, X.; Lassen, R. N.; Jensen, K. H.; Looms, M. C. Monitoring CO_2 migration in a shallow sand aquifer using 3D crosshole electrical resistivity tomography. *International Journal of Greenhouse Gas Control* **2015,** *42*, 534–544.

Zhou, Q.; Yang, X.; Zhang, R.; Hosseini, S. A.; Ajo-Franklin, J. B.; Freifeld, B. M.; Daley, T. M.; Hovorka, S. D. Dynamic Processes of CO_2 Storage in the Field: 1. Multiscale and Multipath Channeling of CO_2 Flow in the Hierarchical Fluvial Reservoir at Cranfield, Mississippi. *Water Resources Research* **2020,** 56. doi:10.1029/2019WR025688.

NRAP is an initiative within DOE’s Office of Fossil Energy and is led by the National Energy Technology Laboratory (NETL). It is a multi-national-lab effort that leverages broad technical capabilities across the DOE complex to develop an integrated science base that can be applied to risk assessment for long-term storage of carbon dioxide (CO_2). NRAP involves five DOE national laboratories: NETL, Lawrence Berkeley National Laboratory (LBNL), Lawrence Livermore National Laboratory (LLNL), Los Alamos National Laboratory (LANL), and Pacific Northwest National Laboratory (PNNL).

Technical Leadership Team

Diana Bacon
Task Lead, Risk Assessment Tools and Methods
Field Validation
Pacific Northwest National Laboratory
Richmond, WA

Chris Brown
PNNL Lab Lead
Pacific Northwest National Laboratory
Richmond, WA

Robert Dilmore
Technical Director, NRAP
NETL Lab Lead
Research and Innovation Center
National Energy Technology Laboratory
Morgantown, WV

Erika Gasperikova
Task Lead, Strategic Monitoring
Lawrence Berkeley National Laboratory
Berkeley, CA

Dylan Harp
Task Lead, Containment Assurance / Leakage Risk
Los Alamos National Laboratory
Berkeley, CA

Curt Oldenburg
LBNL Lab Lead
Lawrence Berkeley National Laboratory
Berkeley, CA

Rajesh Pawar
LANL Lab Lead
Los Alamos National Laboratory
Los Alamos, NM

Tom Richard
Deputy Technical Director, NRAP
The Pennsylvania State University
State College, PA

Megan Smith
LLNL Lab Lead
Lawrence Livermore National Laboratory
Livermore, CA

R. Burt Thomas
Task Lead, Addressing Critical Stakeholder Questions
Research and Innovation Center
National Energy Technology Laboratory
Albany, OR

Josh White
Task Lead, Induced Seismicity Risk Management
Lawrence Livermore National Laboratory
Livermore, CA

Randal Gentry
Deputy Director
Science and Technology Strategic Plans and Programs
National Energy Technology Laboratory
U.S. Department of Energy

Bryan Morreale
Executive Director
Research and Innovation Center
National Energy Technology Laboratory
U.S. Department of Energy

Heather Quedenfeld
Associate Director
Coal Development and Integration
National Energy Technology Laboratory
U.S. Department of Energy

Mark McKoy
Technology Manager (acting)
Strategic Planning
Science and Technology Strategic Plans and Programs
National Energy Technology Laboratory
U.S. Department of Energy

Mark Ackiewicz
Director
Division of Carbon Capture and Storage
Office of Fossil Energy
U.S. Department of Energy

Darin Damiani
Program Manager
Carbon Storage Program
Office of Fossil Energy
U.S. Department of Energy

NRAP Executive Committee

Grant Bromhal
Senior Research Fellow
Geological & Environmental Systems
National Energy Technology Laboratory

Jens Birkholzer
Associate Laboratory Director
Energy and Environmental Sciences
Lawrence Berkeley National Laboratory

George Peridas
Director, Carbon Management Partnerships
Lawrence Livermore National Laboratory

Melissa Fox
Program Manager
Applied Energy Programs
Los Alamos National Laboratory

George Guthrie
Chair, NRAP Executive Committee
Program Manager
Earth and Environmental Sciences
Los Alamos National Laboratory

Alain Bonneville
Laboratory Fellow
Pacific Northwest National Laboratory

Robert Dilmore
Technical Director, NRAP
Research and Innovation Center
National Energy Technology Laboratory